Lecture Notes in Electrical Engineering 388

Jiadong Sun
Jingnan Liu
Shiwei Fan
Feixue Wang
Editors

China Satellite Navigation Conference (CSNC) 2016 Proceedings: Volume I

Springer

Lecture Notes in Electrical Engineering

Volume 388

About this Series

"Lecture Notes in Electrical Engineering (LNEE)" is a book series which reports the latest research and developments in Electrical Engineering, namely:

- Communication, Networks, and Information Theory
- Computer Engineering
- Signal, Image, Speech and Information Processing
- Circuits and Systems
- Bioengineering

LNEE publishes authored monographs and contributed volumes which present cutting edge research information as well as new perspectives on classical fields, while maintaining Springer's high standards of academic excellence. Also considered for publication are lecture materials, proceedings, and other related materials of exceptionally high quality and interest. The subject matter should be original and timely, reporting the latest research and developments in all areas of electrical engineering.

The audience for the books in LNEE consists of advanced level students, researchers, and industry professionals working at the forefront of their fields. Much like Springer's other Lecture Notes series, LNEE will be distributed through Springer's print and electronic publishing channels.

More information about this series at http://www.springer.com/series/7818

Jiadong Sun · Jingnan Liu
Shiwei Fan · Feixue Wang
Editors

China Satellite Navigation Conference (CSNC) 2016 Proceedings: Volume I

Springer

Editors
Jiadong Sun
Chinese Academy of Sciences
China Aerospace Science and Technology Corporation
Beijing
China

Jingnan Liu
Wuhan University
Wuhan
China

Shiwei Fan
China Satellite Navigation Office
Beijing
China

Feixue Wang
National University of Defense Technology
Changsha
China

ISSN 1876-1100 ISSN 1876-1119 (electronic)
Lecture Notes in Electrical Engineering
ISBN 978-981-10-0933-4 ISBN 978-981-10-0934-1 (eBook)
DOI 10.1007/978-981-10-0934-1

Library of Congress Control Number: 2016937343

Printed on acid-free paper

This Springer imprint is published by Springer Nature
The registered company is Springer Science+Business Media Singapore Pte Ltd.

Preface

BeiDou Navigation Satellite System (BDS) is China's global navigation satellite system which has been developed independently. BDS is similar in principle to global positioning system (GPS) and compatible with other global satellite navigation systems (GNSS) worldwide. The BDS will provide highly reliable and precise positioning, navigation and timing (PNT) services as well as short-message communication for all users under all-weather, all-time, and worldwide conditions.

China Satellite Navigation Conference (CSNC) is an open platform for academic exchanges in the field of satellite navigation. It aims to encourage technological innovation, accelerate GNSS engineering, and boost the development of the satellite navigation industry in China and in the world.

The 7th China Satellite Navigation Conference (CSNC2016) is held during May 18–20, 2016, Changsha, China. The theme of CSNC2016 is Smart Sensing, Smart Perception, including technical seminars, academic exchanges, forums, exhibitions, and lectures. The main topics are as follows:

S1 BDS/GNSS Application Technology
S2 Navigation and Location-Based Services
S3 Satellite Navigation Signals
S4 Satellite Orbit and Clock Offset Determination
S5 BDS/GNSS Precise Positioning Technology
S6 Atomic Clock and Time-frequency Technology
S7 BDS/GNSS Augmentation Systems and Technology
S8 BDS/GNSS Test and Assessment Technology
S9 BDS/GNSS User Terminal Technology
S10 Multi-sensor Fusion Navigation
S11 PNT System and Emerging Navigation Technology
S12 Standardization, Intellectual Properties, Policies, and Regulations

The proceedings (Lecture Notes in Electrical Engineering) have 176 papers in ten topics of the conference, which were selected through a strict peer-review process from 440 papers presented at CSNC2016. In addition, another 193 papers

were selected as the electronic proceedings of CSNC2016, which are also indexed by "China Proceedings of Conferences Full-text Database (CPCD)" of CNKI and Wan Fang Data.

We thank the contribution of each author and extend our gratitude to 237 referees and 48 session chairmen who are listed as members of editorial board. The assistance of CNSC2016's organizing committees and the Springer editorial office is highly appreciated.

The 7th China Satellite Navigation Conference (CSNC 2016) Committees

Scientific Committee

Chairman
Jiadong Sun, China Aerospace Science and Technology Corporation

Vice-Chairman
Rongjun Shen, China
Jisheng Li, China
Qisheng Sui, China
Changfei Yang, China
Zuhong Li, China Academy of Space Technology
Shusen Tan, Beijing Satellite Navigation Center, China

Executive Chairman
Jingnan Liu, Wuhan University
Yuanxi Yang, China National Administration of GNSS and Applications
Shiwei Fan, China

Committee Members (By Surnames Stroke Order)
Xiancheng Ding, China Electronics Technology Group Corporation
Qingjun Bu, China
Liheng Wang, China Aerospace Science and Technology Corporation
Yuzhu Wang, Shanghai Institute of Optics and Fine Mechanics, Chinese Academy of Sciences
Guoxiang Ai, National Astronomical Observatories, Chinese Academy of Sciences
Shuhua Ye, Shanghai Astronomical Observatories, Chinese Academy of Sciences
Zhaowen Zhuang, National University of Defense Technology
Qifeng Xu, PLA Information Engineering University
Houze Xu, Institute of Geodesy and Geophysics, Chinese Academy of Sciences
Guirong Min, China Academy of Space Technology

Xixiang Zhang, China Electronics Technology Group Corporation
Lvqian Zhang, China Aerospace Science and Technology Corporation
Junyong Chen, National Administration of Surveying, Mapping and Geoinformation
Benyao Fan, China Academy of Space Technology
Dongjin Luo, China
Guohong Xia, China Aerospace Science and Industry Corporation
Chong Cao, China Research Institute of Radio Wave Propagation (CETC 22)
Faren Qi, China Academy of Space Technology
Sili Liang, China Aerospace Science and Technology Corporation
Shancheng Tu, China Academy of Space Technology
Rongsheng Su, China
Zhipeng Tong, China Electronics Technology Group Corporation
Ziqing Wei, Xi'an Institute of Surveying and Mapping

Organizing Committee

Secretary General
Haitao Wu, Navigation Headquarters, Chinese Academy of Sciences

Vice Secretary General
Wenhai Jiao, China Satellite Navigation Office Engineering Center
Jianjun Wu, National University of Defense Technology
Weina Hao, Navigation Headquarters, Chinese Academy of Sciences

Committee Members (By Surnames Stroke Order)
Qun Ding, The 20th Research Institute of China Electronics Technology Group Corporation
Miao Yu, China Academy of Space Technology
Li Wang, International Cooperation Research Center China Satellite Navigation Engineering Office
Ying Liu, China Satellite Navigation Office Engineering Center
Shuhua Zhang, National University of Defense Technology, Changsha
Xiuwan Chen, Peking University
Xiangan Zhao, China Defense Science and Technology Information Center
Ouyang Guangzhou, Academy of Opto-electronics, Chinese Academy of Sciences
Gang Hu, Beijing Unicore Communications, Inc.
Min Shui, National Remote Sensing Centre of China
Zhong Dou, National Time Service Center, Chinese Academy of Sciences

Editorial Board

Topic S12: Standardization, Intellectual Properties, Policies, and Regulations
Daiping Zhang, China Defense Science and Technology Information Center
Yonggang Wei, China Academy of Aerospace Standardization and Product Assurance
Haibo Liu, Institute of Policy and Management, Chinese Academy of Sciences
Haibo Wang, Electronic Intellectual Property Center, Ministry of Industry and Information Technology, PRC

Contents

Part I
BDS/GNSS Application Technology

The Research on Four-Dimensional Water Vapor Tomography Based on Real-Time PPP Technique

Qingzhi Zhao, Yibin Yao and Chaoqian Xu

Abstract With the development of International GNSS Service (IGS) real-time pilot project (RTPP) acquiring precipitable water vapor (PWV) with high accuracy has become a reality based on the real-time precise point pointing (RT-PPP) technique. The accuracy of zenith total delay (ZTD) and PWV derived from RT-PPP have been validated using observed global positioning system (GPS) data and meteorology data from Satellite Positioning Reference Station Network (SatRef) in 2014. The ZTD comparison with that from afterwards PPP and GAMIT software shows that the relative coefficients are 0.9786 and 0.9687, respectively. The PWV comparison with that from radiosonde shows that the relative coefficient and RMS are 0.9512 and 2.13 mm, respectively. It is a clear evidence that the RT-PPP technique has a similar accuracy with the result calculated using afterwards IGS products. However, PWV is mean of water vapor information of many GNSS signal rays during a period of time over the station, which cannot reflect the three-dimensional water vapor distribution. Slant water vapor (SWV) can be obtained by mapping PWV at different elevation and azimuth angles. The tomographic experiment has been performed using SWVs of twelve stations from SatRef as tomographic observation and compared with result from radiosonde. The comparison shows a good agreement and the RMS, SD, Bias, and MAE of integrated water vapor (IWV) are 3.60, 2.78, 2.29, and 2.92 mm, respectively, the root mean square (RMS), standard deviation (SD), Bias, and mean absolute error (MAE) of calculated water vapor density are 1.08, 1.03, −0.21, and 0.77 g/m^3, respectively. The above result makes it possible that acquiring the real-time three-dimensional water vapor distribution using tomography approach with SWVs derived from RT-PPP technique, which has an important influence on short-term disastrous weather and now-casting precipitation forecasting.

Keywords IGS · Real-time pilot project · Real-time PPP technique · Slant water vapor · Tomography approach

Q. Zhao (✉) · Y. Yao · C. Xu
School of Geodesy and Geomatics, Wuhan University, Wuhan 430072, China
e-mail: zhaoqingzhia@163.com

J. Sun et al. (eds.), *China Satellite Navigation Conference (CSNC) 2016 Proceedings: Volume I*, Lecture Notes in Electrical Engineering 388,
DOI 10.1007/978-981-10-0934-1_1

1 Introduction

In recent years, acquiring three-dimensional/four-dimensional water vapor distribution based on ground-based GNSS tomographic technique has developed significantly [1–5]. The wet refractivity field or water vapor field with high spatial-temporal resolution can be reconstructed by tomography technique using a large number of SWVs which penetrate the whole tomographic area derived from the network of ground-based GNSS. There are two methods for obtaining PWV/SWV using GNSS observed data: PPP technique based on undifferenced observations [6] and baseline/network solving pattern based on double-differenced observations. With the proposed of IGS RTPP [7], users can get real-time products of precise satellite orbit and clock online [8], which promotes the rapid development of RT-PPP technique [9, 10] and makes RT-PPP technique becomes one of the most important tools to get real-time PWV/SWV [11, 12].

The ZTD derived from double-differenced observations is compared with that from numerical forecasting model and radiosonde data, and the accuracy is 6–13 mm [13, 14]. The accuracy of ZTD derived from RT-PPP technique using data provided by GPS system is 11–16 mm, about 2–3 mm PWV error, the accuracy of BDS is slightly lower than that of GPS, but combining data of two systems can get 1.3–1.8 mm PWV error [15]. So, the accuracy of PWV obtained by RT-PPP technique is similar with that of double-differenced technique. However, PWV is an average value of water vapor information of many GNSS signal rays during a period of time over the station, which cannot reflect the three-dimensional water vapor distribution. The emerging of GNSS water vapor tomography technique solves this tricky problem which constrains the application for GNSS meteorology [16]. The real-time three-dimensional wet refractivity or water vapor distribution with high spatial-temporal resolution can be obtained by tomography approach using SWVs derived from RT-PPP technique. This has very important practical significant for improving the accuracy of numerical weather forecasting model, quantified precipitation forecasting and short-term disastrous weather forecasting [17–20].

In this paper, a four-dimensional water vapor monitoring system was designed and developed based on RT-PPP and tomography technique. Simulation experiment has performed based on the observed data of 12 stations from SatRef and obtained a good result.

2 The Method for Acquiring SWV and Theory of Tomography

2.1 The Method for Acquiring SWV

ZTD can be obtained by undifferenced or double-differenced observations; and the popular software package of data processing includes GAMIT/GOBK, Bernese,

GIPSY, EPOS, TriP, and so on. ZTD is the average value which is mapped by many STDs from the slant path to zenith path based on mapping function and consists of two parts: zenith hydrostatic delay (ZHD) and zenith wet delay (ZWD). ZWD is about 10 % of ZTD and ZHD is about 90 % of ZTD [21].

ZWD is relevant with the change of water vapor in troposphere and cannot be modeled accurately. On the contrary, ZHD can be obtained accurately with surface pressure by model, such as Saastamoinen model. The error of ZHD is 0.2 mm when the variation of surface is 1 hPa using Saastamoinen model [22], which meets the requirement of meteorological application. So the ZWD can be extracted from ZTD by minus ZHD. The formula for calculating ZHD using Saastamoinen is as follows: [23]:

$$\mathrm{ZHD}=\frac{0.002277\cdot P_s}{1-0.00266\cdot\cos(2\varphi)-0.00028\cdot H} \tag{2.1}$$

where P_s is surface pressure (unit: hPa), φ is the latitude of station, H is the height of station (unit: km).

Slant wet delay (SWD) can be calculated using mapping function like VMF1, GMF, NMF, the formula as follows:

$$\mathrm{SWD_{A,e}} = \mathrm{M_{wet}(e)\cdot ZWD} + \mathrm{M_{\Delta}(e)\cdot (G^{w}_{NS}\cdot \cos A} + \mathrm{G^{w}_{WE}\cdot \sin A)} + \mathrm{R_e} \tag{2.2}$$

where A is azimuth, e is elevation angle, $\mathrm{M_{wet}}$ is wet mapping function, $\mathrm{M_{\Delta}}$ is the mapping function of horizontal gradient, $\mathrm{G^{w}_{NS}}$ and $\mathrm{G^{w}_{WE}}$ are the horizontal gradient components in East–West and South–North directions, $\mathrm{R_e}$ is unmodeled postfit residuals.

SWD can be converted to SWV by conversion factor as follows: [24]:

$$\mathrm{SWV} = \Pi\cdot \mathrm{SWD} \tag{2.3}$$

where $\Pi = 10^6/((k_2' + k_3/T_m)\cdot R_v\cdot\rho), k_3 = (3.776\pm 0.014)\times 10^5\ \mathrm{K^2\ hPa^{-1}}$, $k_2' = 16.48\ \mathrm{K\ hPa^{-1}}$, are constants, $R_\omega = 461\ (\mathrm{J\ kg^{-1}\ K^{-1}})$ represents water gas ratio constant, ρ is water vapor, T_m represents weighted mean temperature.

2.2 The Theory of Tomography

SWV is relevant with the integrated wet profile of slant path, and represents the total water vapor content of unit area along slant path column (unit: $\mathrm{kg/m^2}$), also equals to the total content of liquid water vapor for the same height (unit: mm) [25]. The definition of SWV is as follows:

$$\mathrm{SWV} = \int_S \rho_v \mathrm{d}s \tag{2.4}$$

where s represents the path of the satellite signal ray, ρ_v represents water vapor density (unit: g/m^3). A linear equation between SWV and water vapor density can be established:

$$\mathrm{SWV}^p = \sum_{ijk} \left(\mathrm{A}_{ijk}^p \cdot \mathrm{X}_{ijk}\right) \tag{2.5}$$

where SWV^p is the slant water vapor amount of the pth signal ray (unit: mm); A_{ijk}^p is the distance of the pth signals ray inside the (i,j,k) voxel; X_{ijk} is the water vapor density in the voxel (i,j,k) (unit: g/m^3). The above equation can then be written in matrix form as follows:

$$\boldsymbol{y} = \boldsymbol{A} \cdot \boldsymbol{x} \tag{2.6}$$

where $\boldsymbol{y}$ is a column vector with a set of SWV measurements, $\boldsymbol{A}$ is a coefficient matrix with the element of distance, $\boldsymbol{x}$ is a column vector of unknown water vapor density. In our study, an elevation cut off angle of 10° for signals of every receiver is selected in order to ignore the influence of ray bending [26, 27].

It can be seen from above equation that the nature of solving the unknown water vapor density is an issue of inversion algorithm. The design matrix $\boldsymbol{A}$ in Eq. (2.6), however, is a large sparse matrix and many voxels are not crossed by signal rays. The normal equation of $\boldsymbol{A}$ is singular which leads to severe numerical problems when applying a direct inversion method [28]. Some constraint conditions are often introduced to the tomography equation [16, 29]. In our study, the Gauss-weighted functional method is used in the horizontal direction [30], while in the vertical direction the function relationship of exponential distribution is established [31]. Finally, the tomography model is then acquired as

$$\begin{pmatrix} \boldsymbol{A}_{l\times n}^{\mathrm{slant}} \\ \boldsymbol{A}_{m\times n}^{\mathrm{zenith}} \\ \boldsymbol{H}_{l\times n} \\ \boldsymbol{V}_{l\times n} \end{pmatrix} \cdot \boldsymbol{x}_{n\times 1} = \begin{pmatrix} \boldsymbol{SWV}_{l\times 1} \\ \boldsymbol{PWV}_{m\times 1} \\ \boldsymbol{0}_{l\times 1} \\ \boldsymbol{0}_{l\times 1} \end{pmatrix} \tag{2.7}$$

where $\boldsymbol{A}_{l\times n}^{\mathrm{slant}}$ is mapping function in the slant direction, $\boldsymbol{A}_{m\times n}^{\mathrm{zenith}}$ is mapping function in the vertical direction, $\boldsymbol{H}$ and $\boldsymbol{V}$ are the coefficient matrixes for the horizontal and vertical constraints, respectively.

3 Data Introduction and Accuracy Analysis of RT-PPP

3.1 Data Introduction

Data of twelve stations derived from SatRef in Hong Kong has been selected for tomographic experiment, and the distance between two neighboring stations is about 10–15 km, the geographic location for every station is shown by ▲ in Fig. 1. All stations are equipped with meteorological sensors and the real-time meteorological parameters can also be obtained. It is reported that accuracies of surface pressure and temperature are better than ±0.08 hPa and ±0.2 °C, respectively, and surface relative humidity is better than ±02 % at 25 °C (More information in http://www.paroscientific.com/pdf/met4DataSheet.pdf). The real-time observed GPS data and meteorological data can be downloaded from the website (http://www.geodetic.gov.hk/smo/gsi/programs/en/GSS/satref/satref.htm) with the interval of 5 s and 1 min, respectively. There is a radiosonde station in King's Park which is shown by ● in Fig. 1, and the water vapor profile in the vertical direction with high accuracy can be obtained using recorded radiosonde data [21, 32, 33]. These data can be freely downloaded afterwards from website (ftp://ncdc.noaa.gov/pub/data/igra/), which recorded the data of UTC 00:00 and 12:00 every day.

3.2 Accuracy Analysis of RT-PPP ZTD

The accuracy of ZTD processed by GAMIT software using GPS data is better than ±1 cm [34], in this paper, it is regarded as a reference to validate the ZTD calculated by RT-PPP technique. In addition, the result calculated by PPP technique using afterwards precise products of orbit and clock provided by IGS is also used to test the result of RT-PPP technique. Data of twelve stations are processed using

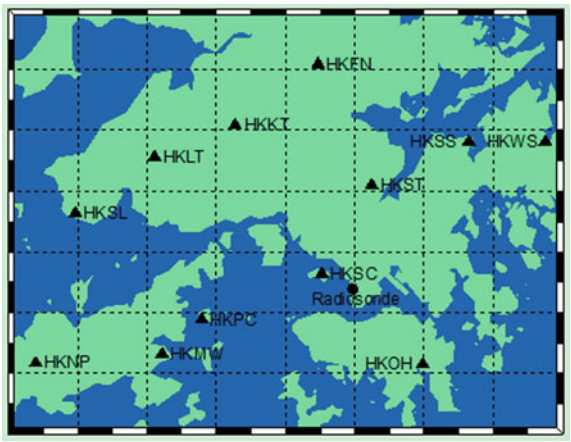

Fig. 1 Location of stations, *filled triangle* represents GPS station and *filled circle* represents radiosonde station

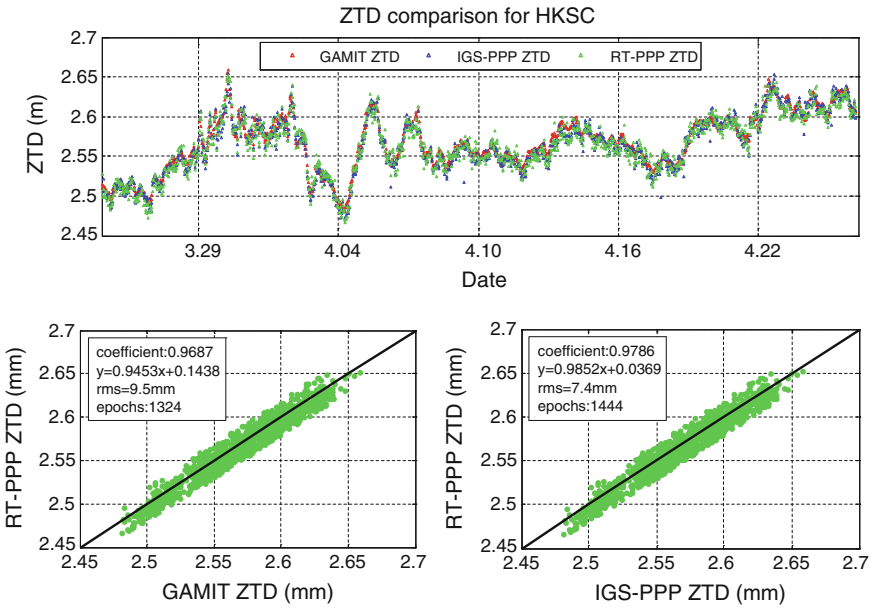

Fig. 2 Comparison of ZTD derived from real-time PPP, GAMIT software and IGS-PPP for HKSC (Color figure online)

GAMIT10.5 software, Fig. 2 gives the ZTD comparison once every half an hour derived from different methods for HKSC station.

It can be seen from Fig. 2 that the changed trend of ZTD is consistent between RT-PPP, IGS-PPP, and GAMIT. For the statistical result of 32 days, the coefficient of ZTD calculated by RT-PPP technique with IGS-PPP technique and GAMIT software are 0.9687 and 0.9786, respectively, and the RMS are 9.5 and 7.4 mm, respectively. This shows that the ZTD accuracy of RT-PPP technique is the same with afterwards processed result.

3.3 Accuracy Analysis of RT-PPP PWV

Radiosonde is one of the most effective ways to obtain PWV with high accuracy in the vertical direction, and there is a radiosonde 45,004 about 2.4 km far away from HKSC station in experiment area. It has been proved that the horizontal change of water vapor in the troposphere can be neglected between two stations [4]. Therefore, the result derived from radiosonde data is regarded as a reference to validate the accuracy of RT-PPP technique. First, the radiosonde data from March 25, 2014 to April 25, 2014 for UTC 00:00 and 12:00 is processed and the PWV is obtained for specific epochs. Figure 3 shows the PWV comparison between different methods.

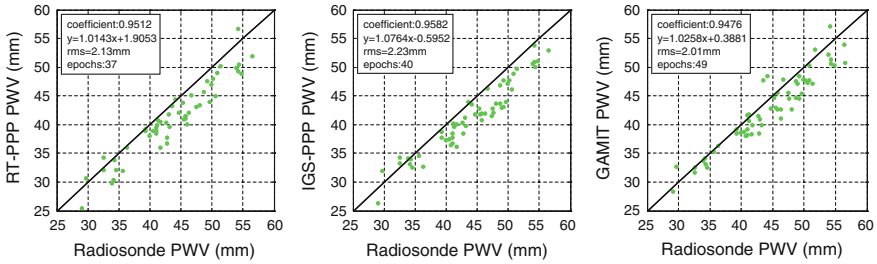

Fig. 3 Comparing PWV retrieved from GPS data with that calculated from radiosonde data for HKSC

Figure 3 is an evidence that the PWV calculated by RT-PPP technique has a consistency with that from radiosonde. The statistical result shows that the coefficients of radiosonde with RT-PPP, IGS-PPP and GAMIT are 0.9512, 0.9582, and 0.9476, respectively, and the RMS are 2.13, 2.23, and 2.01 mm, respectively. This result reaches the accuracy level that can be achieved internationally [25, 35, 36]. With this we can conclude that the PWV accuracy derived from RT-PPP technique is the same with the result that is processed afterwards.

4 Comparison of Tomographic Result

4.1 Introduction of Tomographic Experiment

The range of the tomographic area is as follows: latitude from 22.19°N to 22.54°N and longitude from 113.87°E to 114.35°E. Voxel division: horizontal resolution in longitude and latitude are 0.06° and 0.05°, respectively, and vertical resolution is 0.8 km. The total number of voxels is 7 × 8 × 13. The observed data of twelve stations (as shown by ▲ in Fig. 1) are selected for tomographic experiment.

4.2 IWV Comparison

Radiosonde data can provide accurate water vapor density profile in vertical direction [21], and IWV is the integral of water vapor along the vertical direction above the radiosonde station. The IWV derived from radiosonde and tomographic result is compared for the location of radiosonde (see Fig. 4). It can be seen from Fig. 4 that the changed trend of IWV for two methods is similar. By calculation, the RMS, SD, Bias and MAE of IWV are 3.6, 2.78, 2.29, and 2.92 mm, respectively.

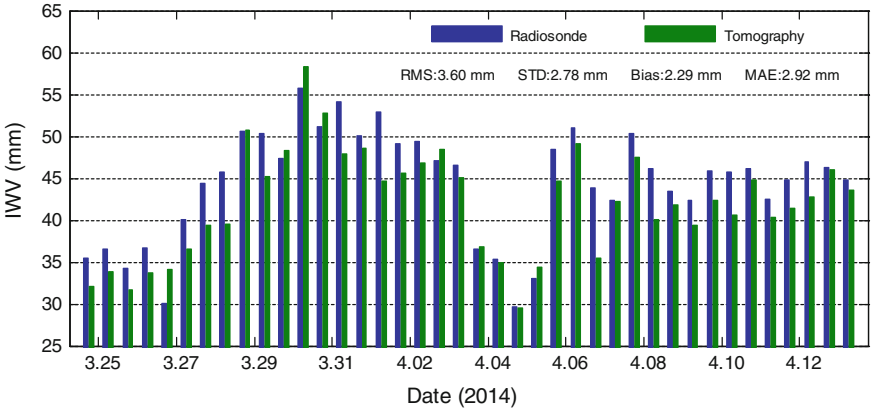

Fig. 4 Comparison of IWV time series derived from radiosonde and tomographic result (Color figure online)

4.3 Comparison of Layered Water Vapor

Although IWV result derived from tomographic result agrees well with those from the radiosonde, while also showing lower RMS, SD, MAE, and Bias, one may not conclude that the vertical water vapor distribution profile has been obtained correctly. For instance, if two vertical layers are exchanged arbitrarily, the calculated IWV value remains unchanged, but the vertical distribution of water vapor changes. Therefore, in order to further test the accuracy of vertical water vapor density, 40 epochs of tomographic period are analyzed. Figure 5 gives the tomographic result with that of radiosonde for different layers. We can see that the distributed water vapor density agrees well with that from radiosonde data. By calculation, the RMS of water vapor density is 1.08 g/m^3, which means tomographic water vapor density has high accuracy in the vertical direction.

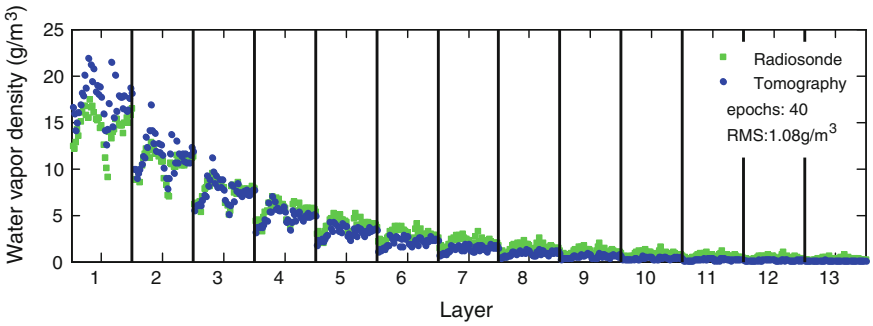

Fig. 5 Tomographic result comparison with water vapor density from radiosonde (*green*) for various layers, against water vapor density from tomography (*blue*) for 40 epochs spanning from March 25, 2014 to April 13, 2014 (color figure online)

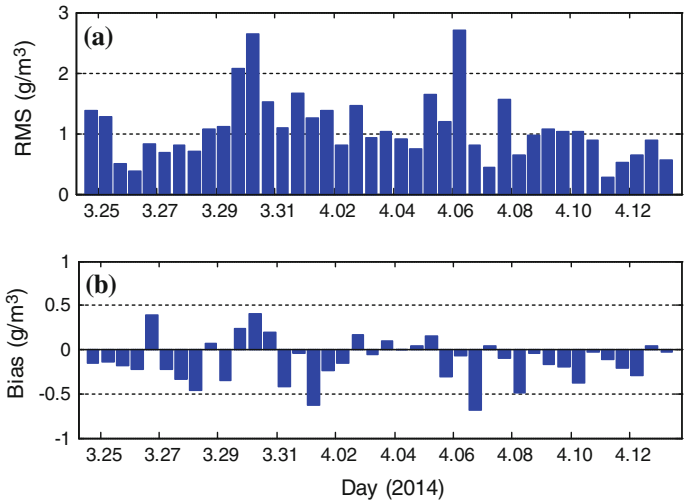

Fig. 6 Distribution of RMS and Bias for tomographic result

Table 1 Statistical result between radiosonde and tomographic result (unit: g/m^3)

Data comparison	RMS	SD	Bias	MAE
Tomography versus radiosonde	1.08 [0.28 2.70]	1.03 [0.25 2.70]	−0.12 [−0.68 0.41]	0.77 [0.23 1.84]

In addition, the tomographic result for every day is also analyzed, and the RMS and Bias (see Fig. 6) and statistical result for 20 days (see Table 1) are obtained. The average RMS, SD, Bias, and MAE of tomographic water vapor density are 1.08, 1.03, −0.21, and 0.77 g/m^3, respectively, which means that the accuracy of tomographic result is good.

5 Conclusion

In this paper, a four-dimensional water vapor tomography method has been proposed based on the RT-PPP technique. The accuracy of ZTD and PWV derived from RT-PPP technique is first validated using data from March 25, 2014 to April 25, 2014. On comparing the results of PPP technique, GAMIT software, and radiosonde, it shows that RT-PPP technique is capable of acquiring ZTD and PWV with the same accuracy of results that are processed afterwards. SWVs are calculated based on RT-PPP technique, and regarded as tomographic observation.

Tomographic experiment has been performed using twenty days' data of twelve stations from SatRef and obtained a good result. It is evident that the real-time three-dimensional water vapor distribution obtained based on RT-PPP technique is of many potential application values, especially for those timeliness strong weather forecasting like short-term precipitation forecasting and real-time precipitation forecasting. Consequently, the research on four-dimensional water vapor tomography based on RT-PPP technique has very important research significance.

Acknowledgements The authors would like to thank IGAR for providing access to the web-based IGAR data. The Lands Department of HKSAR is also acknowledged for providing GPS data from the Hong Kong Satellite Positioning Reference Station Network (SatRef) and meteorological data.

References

1. Bastin S, Champollion C, Bock O, Drobinski P, Masson F (2005) On the use of GPS tomography to investigate water vapor variability during a Mistral/sea breeze event in southeastern France. Geophys Res Lett 32(5)
2. Lutz SL (2008) High-resolution GPS tomography in view of hydrological hazard assessment. Doctoral dissertation, Diss., Eidgenössische Technische Hochschule ETH Zürich, Nr. 17675
3. Champollion C, Flamant C, Bock O, Masson F, Turner DD, Weckwerth T (2009) Mesoscale GPS tomography applied to the 12 June 2002 convective initiation event of IHOP 2002. QJR Meteorol Soc 135:645–662
4. Jiang P, Ye SR, Liu YY, Zhang JJ, Xia PF (2014) Near real-time water vapor tomography using ground-based GPS and meteorological data: long-term experiment in Hong Kong. In: Annales Geophysicae, vol 32(8). Copernicus GmbH, pp 911–923
5. Adavi Z, Mashhadi-Hossainali M (2014) 4D tomographic reconstruction of the tropospheric wet refractivity using the concept of virtual reference station, case study: northwest of Iran. Meteorol Atmos Phys 126(3–4):193–205
6. Zumberge JF, Heflin MB, Jefferson DC, Watkins MM, Webb FH (1997) Precise point positioning for the efficient and robust analysis of GPS data from large networks. J Geophys Res Solid Earth (1978–2012) 102(B3):5005–5017
7. Dow JM, Neilan RE, Rizos C (2009) The international GNSS service in a changing landscape of global navigation satellite systems. J Geod 83(3–4):191–198
8. Caissy M, Agrotis L, Weber G, Hernandez-Pajares M, Hugentobler U (2012) Coming soon: the International GNSS real-time service. GPS World 23(6):52–58
9. Li X, Zhang X, Ge M (2011) Regional reference network augmented precise point positioning for instantaneous ambiguity resolution. J Geod 85(3):151–158
10. Li X, Ge M, Zhang H, Nischan T, Wickert J (2013) The GFZ real-time GNSS precise positioning service system and its adaption for COMPASS. Adv Space Res 51(6):1008–1018
11. Li X, Dick G, Ge M, Heise S, Wickert J, Bender M (2014) Real-time GPS sensing of atmospheric water vapor: precise point positioning with orbit, clock, and phase delay corrections. Geophys Res Lett 41(10):3615–3621
12. Dousa J, Vaclavovic P (2014) Real-time zenith tropospheric delays in support of numerical weather prediction applications. Adv Space Res 53(9):1347–1358
13. Haase J, Ge M, Vedel H, Calais E (2003) Accuracy and variability of GPS tropospheric delay measurements of water vapor in the western Mediterranean. J Appl Meteorol 42(11): 1547–1568

14. Gendt G, Dick G, Reigber C, Tomassini M, Liu Y, Ramatschi M (2004) Near real time GPS water vapor monitoring for numerical weather prediction in Germany. J Meteorol Soc Jpn 82 (1B):361–370
15. Lu C, Li X, Nilsson T, Ning T, Heinkelmann R, Ge M, Schuh H (2015). Real-time retrieval of precipitable water vapor from GPS and BeiDou observations. J Geod 1–14
16. Flores A, Ruffini G, Rius A (2000) 4D tropospheric tomography using GPS slant wet delays. In: Proceedings of Annales Geophysicae, vol 18(2). Springer, Heidelberg, pp 223–234
17. Emanuel K, Raymond D, Betts A, Bosart L, Bretherton C, Droegemeier K, Thorpe A (1995) Report of the first prospectus development team of the US weather research-program to NOAA and the NSF
18. Bauer HS, Wulfmeyer V, Schwitalla T, Zus F, Grzeschik M (2011) Operational assimilation of GPS slant path delay measurements into the MM5 4DVAR system. Tellus A 63(2):263–282
19. Chen B, Liu Z (2014) Voxel-optimized regional water vapor tomography and comparison with radiosonde and numerical weather model. J Geod 88(7):691–703
20. Yuan Y, Zhang K, Rohm W, Choy S, Norman R, Wang CS (2014) Real-time retrieval of precipitable water vapor from GPS precise point positioning. J Geophys Res Atmos 119 (16):10044–10057
21. Niell AE (2001) Preliminary evaluation of atmospheric mapping functions based on numerical weather models. Phys Chem Earth Part A 26(6):475–480
22. Tregoning P, Herring TA (2006) Impact of a priori zenith hydrostatic delay errors on GPS estimates of station heights and zenith total delays. Geophys Res Lett 33(23)
23. Saastamoinen J (1972). Atmospheric correction for the troposphere and stratosphere in radio ranging satellites. Use Artif Satell Geod 247–251
24. Bevis M, Businger S, Chiswell S, Herring TA, Rocken C, Ware RH (1994) GPS meteorology: mapping zenith wet delays onto precipitable water. J Appl Meteorol 33:379–386
25. Benevides P, Catalao J, Miranda PMA (2015) On the inclusion of GPS precipitable water vapour in the nowcasting of rainfall
26. Bevis M, Businger S, Herring T, Rocken C, Anthes R, Ware R (1992) GPS meteorology: remotesensing of atmospheric water vapor using the global positioningsystem. J Geophys Res 97(D14):15787–15801
27. Mendes VB (1999) Modeling the neutral-atmosphere propagation delay in radiometric space technique. PhD dissertation, University of New Brunswick, Frederiction, New Brunswick
28. Bender M, Stosius R, Zus F, Dick G, Wickert J, Rabe A (2010) GNSS water vapor tomography-Expected improvements by combing GPS, GLONASS and Galileo observations. Adv Sp Res 47:886–897
29. Bender M, Dick G, Ge M, Deng Z, Wickert J, Kahle HG, Tetzlaff G (2011) Development of a GNSS watervapour tomographysystem using algebraic reconstruction techniques. Adv Sp Res 47:1704–1720. doi:10.1016/j.asr.2010.05.034
30. Song SL, Zhu YW, Ding JC et al (2005) Shanghai GPS network tomography vapor three-dimensional distribution to improve numerical forecast humidity field. J Chin Sci Bull 50(20):2271–2277
31. Elósegui P, Ruis A, Davis JL, Ruffini G, Keihm SJ, Bürki B, Kruse LP (1998) An experiment for estimation of the spatial and temporal variations of water vapor using GPS data. Phys Chem Earth 23(1):125–130
32. Adeyemi B, Joerg S (2012) Analysis of water vapor over nigeria using radiosonde and satellite data. J Appl Meteorol Climatol 51:1855–1866. doi:10.1175/JAMC-D-11-0119.1
33. Liu ZZ, Wong MS, Nichol J, Chan PW (2013) A multi-sensor study of water vapour from radiosonde, MODIS and AERONET: a case study of Hong Kong. Int J Climatol 33:109–120. doi:10.1002/joc.3412
34. Gusfarienza H, Yuwono BD, Awaluddin M et al (2015) Penentuan zenith tropospheric delay dan precipitable water vapor Menggunakan Perangkat Lunak Gamit. Jurnal Geodesi Undip 4 (2):78–86

35. Seco A, Ramírez F, Serna E, Prieto E, García R, Moreno A, Priego JE (2012) Rain pattern analysis and forecast model based on GPS estimated atmospheric water vapor content. Atmos Environ 49:85–93
36. de Ortiz Galisteo JP, Bennouna Y, Toledano C, Cachorro V, Romero P, Andrés MI, Torres B (2014) Analysis of the annual cycle of the precipitable water vapour over Spain from 10-year homogenized series of GPS data. Q J R Meteorol Soc 140(679):397–406

A Spread Spectrum Communication Method Based on GNSS Positioning and Timing System

Jie Zhang, Zhaorui Wang and Qingtao Wan

Abstract Application of spread spectrum technology can effectively solve the problem of power constraints in satellite communication. A difficulty of spread spectrum communication is fast acquisition of spread spectrum signal. For the lack of priori information, code phase and frequency offset are both random quantities, it usually takes a long time in signal acquisition, which would reduce the efficiency of the communication especially for the burst communication. Traditional methods realized spread spectrum signal fast acquisition at the expense of acquisition algorithm complexity and hardware resources cost. This article presents a low cost new code phase and carrier frequency of spread spectrum signal correction method that is easy to implement based on GNSS positioning and timing system. In order to correct the frequency offset and code phase difference, position and time information given by GNSS system are used to build the network-wide time synchronization system and indirect loopback correction system in ground station. At the same time, with the aid of satellite timing, the influence of clock error is eliminated in the way of DDS. With the above measures, the spread spectrum signal fast acquisition could be realized in the network-wide time synchronization system.

Keywords Spread spectrum communication · Timing · Time synchronization

1 Introduction

Due to the high orbit satellite, propagation loss of satellite communication system, especially in the GEO satellite communication system is great. Meanwhile, in order to avoid interference between satellite and ground communication systems, low satellite antenna EIRP and weak signal power reaching the ground are obstacles to terminal miniaturization and communication capacity expansion. The spread spectrum technology can effectively solve the problem of limited power in satellite

J. Zhang (✉) · Z. Wang · Q. Wan
National Astronomical Observatories, Chinese Academy of Sciences, Beijing, China
e-mail: zhangjie05@mails.ucas.ac.cn

J. Sun et al. (eds.), *China Satellite Navigation Conference (CSNC) 2016 Proceedings: Volume I*, Lecture Notes in Electrical Engineering 388,
DOI 10.1007/978-981-10-0934-1_2

communication channel with sufficient bandwidth. To comply with International Telecommunication Union (ITU) regulations on signal strength (see [1]), spread spectrum communication technology is used to reduce the wave flux density in the unit band by broadening signal bandwidth for the power. At the same time, the spread spectrum communication has the advantage of confidential, and strong antijamming capability.

Synchronization is a key problem for spread spectrum signal receiving processing. PN code and carrier, at both transmitting and receiving ends should be kept under synchronization, including the synchronization of phase and frequency. At the receiving end, the rough code phase and carrier frequency offset estimation are given by capturing and coarse synchronization. Then the results of coarse synchronization are used to initialize tracking loop and precise synchronization, finally restore the information. As a result, the capture of the spread spectrum signal with high rate and long PN code period is very difficult in high dynamic, low SNR environments.

There are several capture normal methods [2, 3]: sliding correlator, capture time is proportional to the square of PN code period; matching filter, with a short capturing time at great hardware expense. These two methods are 2-D search for code phase and carrier frequency, and affected by the frequency offset. Besides the above two methods, FFT based on carrier frequency is able to overcome the frequency offset on the influence of PN code, but adaptive threshold adjustment for large signal strength varies and increases the complexity of the system.

From the above, for the lack of prior information, the capture of PN code phase and frequency offset value which is random costs a large amount of computation and hardware resources, repeated threshold judgement and adjustment are necessary for the probability of signal capture. Therefore, capture process with a long time reduces the communication efficiency especially for burst communication.

In this study, a new PN code phase and carrier frequency offset correction method based on the link of "Ground station—GEO satellite—Remote station" is proposed. In order to spread spectrum signal fast acquisition, the code phase difference, carrier Doppler frequency offset and clock error are corrected with the aid of GNSS satellite navigation system positioning and timing functions.

2 Construction of Network-Wide Time Synchronization System

In order to improve communication efficiency and user management, network-wide time synchronization technology has been widely used in ground-based 3G and 4G mobile communication system. Time synchronization between the base station (BS) is achieved by GPS or IEEE 1588v2 time transfer technology [4]. The mobile station (MS) achieves time synchronization with BS by time correction parameter in synchronous channel. The 3G and 4G mobile communication networks' time

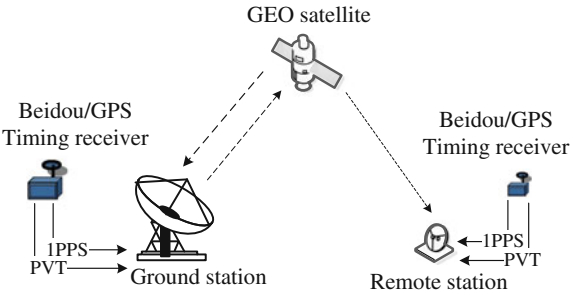

Fig. 1 Network-wide time synchronization system

synchronization precision index is only for μs [4], which is inadequate for the military and security spread spectrum communication with high spreading gain and PN code rate (Mcps). Timing function of Beidou/GPS satellite navigation system with the precision of 20–100 ns could be used as a unified time reference. The signal is transmitted and received under the unified time reference (1PPS). The capture process is accelerated by PVT (position, velocity, time) parameters. The original ground station and remote station are equipped with Beidou/GPS timing receivers to construct the network-wide time synchronization system (Fig. 1).

3 Synchronization of Spread Spectrum Signal

Prerequisites for spread spectrum communication are carrier and PN code synchronization, which means synchronization of both frequency and phase. Code phase, carrier frequency offset, and clock error are corrected, respectively, based on Beidou/GPS positioning and timing system.

3.1 Correction of PN Code Phase Offset

Code phase consists mainly of link propagation delay and equipment delay, which is corrected in different ways, respectively, at ground station and remote station.

3.1.1 Code Clock Round-Trip Link Indirect Correction in Ground Station

In Fig. 1, an example of a communication link composed of "Ground station—GEO satellite—Remote station", round-trip correction link consists of transceiver baseband, RF equipments at ground station, (up/down converter, PA, LNA, and antenna) and GEO satellite, as shown in Fig. 2.

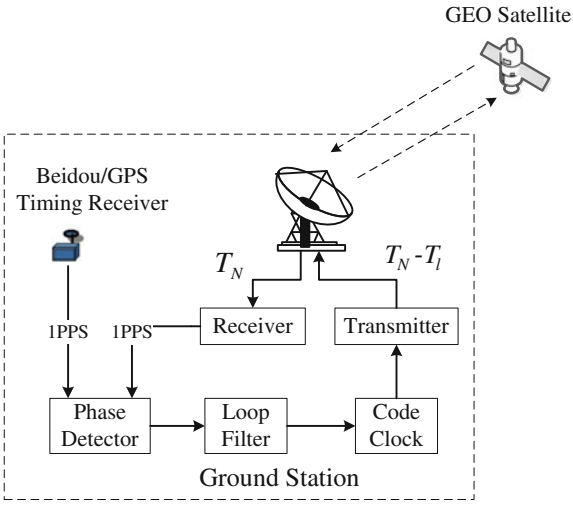

Fig. 2 Principle of code clock indirect loop back correction

The ground station transmits the spread spectrum signal and then receives the signal through the round-trip link. The receiver baseband output 1PPS on the start rising at the edge of each 1 s frame. The phase difference between 1PPS of Beidou/GPS receiver and 1PPS the receiver output is given by phase detector, which is used to feedback the correction of transmitting code clock after loop filter. Through the above indirect adjustment method, data transmitted from the ground station arrives at the receiving end on the rising edge of 1PPS, which means that the data transmitted at the time of $T_N - T_l$ arrives at T_N through round-trip link (T_N is integer second, T_l is the link propagation and equipment delay).

The experiments based on satellite ground link composed of equipments in Fig. 1 verify the above program. The Beidou/GPS timing receiver HM-1103C from Hwa Create Corporation [5]; the ground station located in navigation and communication central station of National Astronomical Observatory in Wuqing district, Tianjin; GEO satellite is a retired commercial satellite. The measured results of 1PPS synchronization precision in actual satellite ground round-trip link are shown in Fig. 3.

The 1PPS synchronization error that is corrected by the ground-satellite round-trip loop gradually converges with 1σ error of 34 ns.

3.1.2 Code Phase Correction in Remote Station

For the communication system in Fig. 1, the 1PPS in the ground-satellite round-trip loop is synchronized with Beidou/GPS 1PPS, but for signal transmitted from the ground station, there is time difference (ΔT) between the time arriving at the ground station and the remote station as the two different down links ("satellite—ground station" and "satellite—remote station").

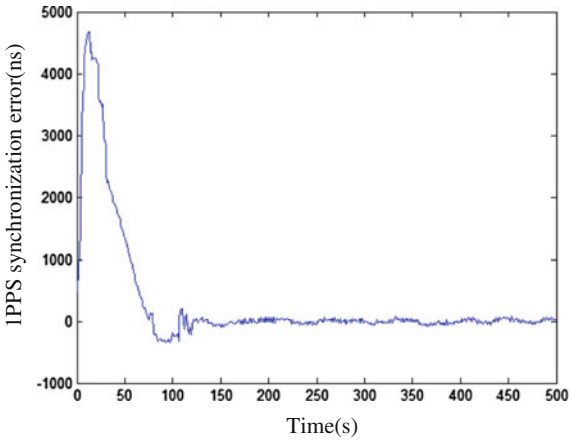

Fig. 3 Receiver-Beiou/GPS output 1PPS synchronization error of the round-trip link

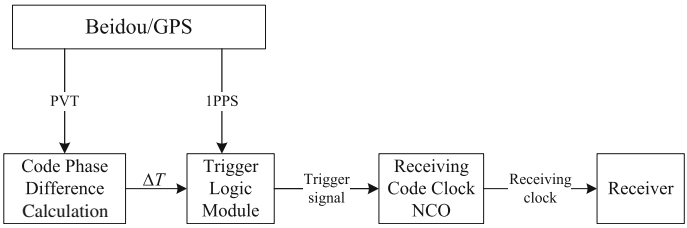

Fig. 4 Correction of propagation time delay difference correction

According to the output of the Beidou/GPS timing receiver position coordinates, precise satellite ephemeris parameters and ground station coordinates, the remote station can calculate the down link propagation delay difference ΔT.

Modules for propagation delay difference correction are shown in Fig. 4.

The propagation time delay difference ΔT can be calculated by real-time computing with Beidou/GPS 1PPS output. The work timing sequence is shown in Fig. 5. The ground station transmits the signal at the time of $T_N - T_l$ (T_N is integer second, T_l is the ground-satellite round-trip propagation and equipment delay), the remote station starts receiving the clock to correlate at the time of $T_N + \Delta T$.

For the "Ground station—GEO satellite—Remote station" link, the code phase difference correction of whole link consists of the above two processes. The remote station code clock starts at a fixed time to receive, so as to, improve the efficiency without signal acquisition process.

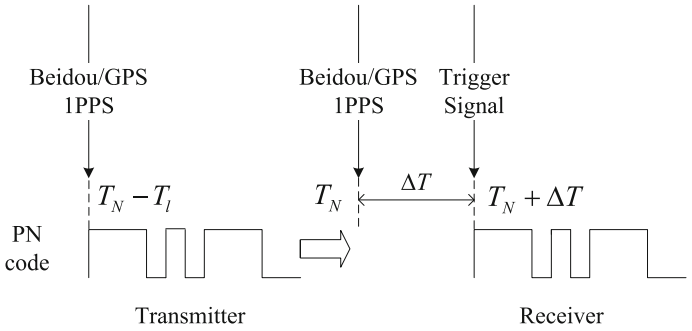

Fig. 5 Propagation time delay difference correction of remote station

3.1.3 Total Code Phase Error

Total code phase error ΔT_s is composed of timing error caused by Beidou/GPS positioning error ΔT_p and 1PPS synchronization error of ground-satellite round-trip link loop ΔT_l. Beidou/GPS positioning precision ΔP is about 10–20 m, c is propagation velocity of electromagnetic wave, then

$$\Delta T_p = \Delta P / c \tag{1}$$

According to the test results, 1PPS synchronization error of ground-satellite round-trip link loop ΔT_l is 34 ns, and the total code phase error is as follows:

$$\Delta T_s = \sqrt{(\Delta T_p)^2 + (\Delta T_l)^2} \tag{2}$$

According to Eq. (2), total code phase correction error ΔT_s is 50–70 ns. The code phase synchronization error should be within $\frac{1}{2}$ code chip for the capture of the PN code. Thus, this program meets the highest code rate 10 Mcps spread spectrum communication capture requirements.

3.2 Carrier Frequency Offset Correction

Carrier frequency offset is composed of Doppler, transformer, and clock error.

3.2.1 Frequency Offset Correction in Ground-Satellite Round-Trip Link

The same way as the code phase correction in Fig. 2, the frequency offset of the forward link is corrected in the ground-satellite round-trip link. In order to keep the

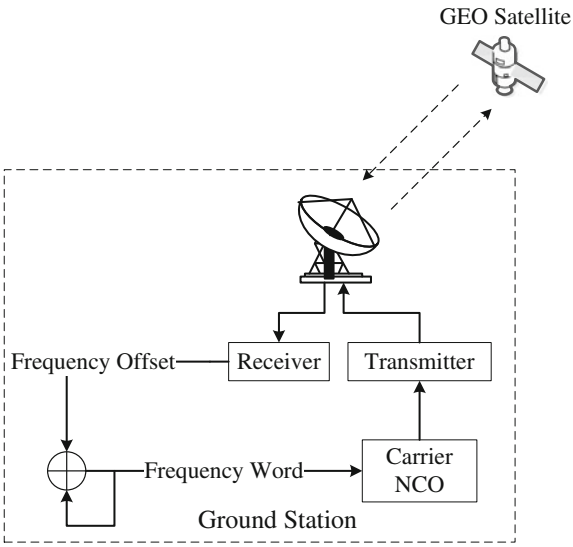

Fig. 6 Principle of frequency offset correction

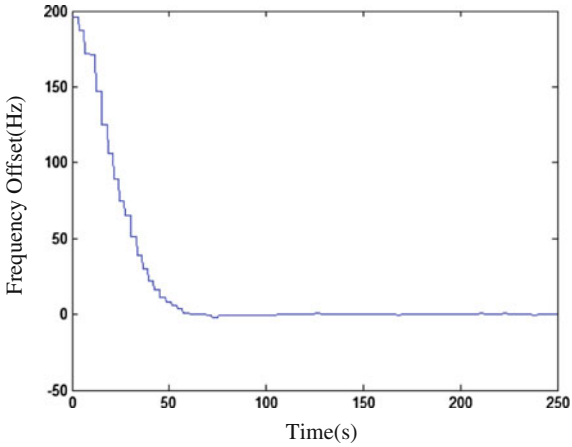

Fig. 7 Results of frequency offset correction

down link frequency at nominal value, as shown in Fig. 6, the receiver outputs the frequency offset to the transmitter for transmitting frequency pre-bias by the closed loop correction.

The results of frequency offset round-trip loop correction finally converge to 0 Hz, as shown in Fig. 7:

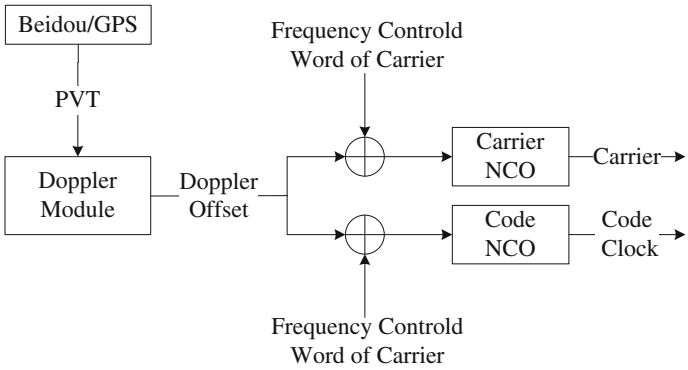

Fig. 8 Consisting of Doppler frequency offset correction

3.2.2 Frequency Doppler Correction in Remote Station

Doppler frequency offset is derived from the relative motion of the carrier. For "Ground station—GEO Satellite—Remote Station" the relative motion of the carrier including the remote station motion and satellite drift can result in frequency offset of the carrier and the code clock.

According to the location coordinates velocity of Beidou/GPS timing receiver output, Doppler carrier and code frequency offset Δf could be calculated, and then, Δf and precise satellite ephemeris are used to frequency pre-bias of carrier and code NCO. The Doppler carrier and code frequency offset Δf is calculated as follows: [6]:

$$\Delta f = -f_T \frac{\left(\overrightarrow{v_d} \cdot \overrightarrow{a}\right)}{c} \tag{3}$$

f_T, nominal frequency of the transmitted signal; $\overrightarrow{v_d}$, relative velocity vector of the transmitting and receiving ends.

$$\overrightarrow{v_d} = \overrightarrow{v_t} - \overrightarrow{v_r} \tag{4}$$

$\overrightarrow{v_t}$, velocity vector of the transmitting end; $\overrightarrow{v_r}$, velocity vector of the receiving end; $\overrightarrow{a}$, unit vector along the straight line from the receiving end to the transmitting end.

$$\overrightarrow{a} = \left(\overrightarrow{u_t} - \overrightarrow{u_r}\right) / \left\|\overrightarrow{u_t} - \overrightarrow{u_r}\right\| \tag{5}$$

$\overrightarrow{u_t}$, location vector of the transmitting end; $\overrightarrow{u_r}$, location vector of the receiving end; $\|\cdot\|$, distance between transmitting and receiving ends; $\overrightarrow{v_d} \cdot \overrightarrow{a}$, radial component of relative velocity vector along the straight line from the receiving end to the transmitting end; c, propagation velocity of electromagnetic wave.

The structure of the Doppler frequency offset correction module as shown in Fig. 8.

For the "Ground station—GEO Satellite—Remote Station" link, frequency of uplink and downlink are as follows:

$$f'_u = f_u + \Delta f_u \tag{6}$$

$$f'_d = f_d + \Delta f_d \tag{7}$$

f_u, nominal frequency of uplink; f_d, nominal frequency of downlink; Δf_u, frequency offset of uplink; Δf_d, frequency offset of downlink. Frequency of uplink is corrected to nominal value f_u frequency pre-bias at the transmitting end; Frequency of downlink is corrected to actual value f'_d at the receiving end.

The above methods apply to "Ground station—GEO Satellite—Remote Station" link, for the reverse link, the code phase difference and frequency offset can be calculated according to PVT parameters at remote station.

3.2.3 Clock Error Correction

Clock error of oscillator at transceiver both ends is also an important cause of frequency offset besides Doppler motion. OCXO is of high stability, but higher cost is not suitable for the terminal equipment. TCXO is of short-term stability but frequency drift for long time, while GNSS timing short-term stability is poor, but of high long-term stability. Therefore, combining the advantages of both TCXO and GNSS timing can be used to the frequency offset correction, which is "discipline". The principle of "discipline" is to adjust the local oscillator according to the frequency error of clock signal generated by local oscillator and determined frequency signal, for both short-term and long-term stability [7, 8].

In this study, a correction method of low cost based on direct digital synthesizer (DDS) with aid of satellite timing is proposed. Specific as follows: GNSS output 1PPS as gating signals, the local clock error Δx of the actual and nominal value could be estimated according to the clock cycles between the two adjacent 1PPS. Then code clock and carrier frequency offset caused by clock error Δx could be corrected by pre-bias. Principle of DDS is as follows [9]:

$$\mathrm{FTW} = \frac{f_o}{2^M}\left(f_{\mathrm{sys}} + \Delta x\right) \tag{8}$$

FTW, the frequency tuning word; f_o, the output frequency; M, the length of the phase accumulator; f_{sys}, nominal frequency of the oscillator.

Structure of clock error correction module is shown in Fig. 9: the local clock error Δx could be estimated according to the clock cycles between gating Beidou/GPS 1PPS signals. In order to avoid the short-term unstability of Beidou/GPS 1PPS, filter the counting results using weighted filtering algorithm. The principle of weighted filtering algorithm is as follows [10]:

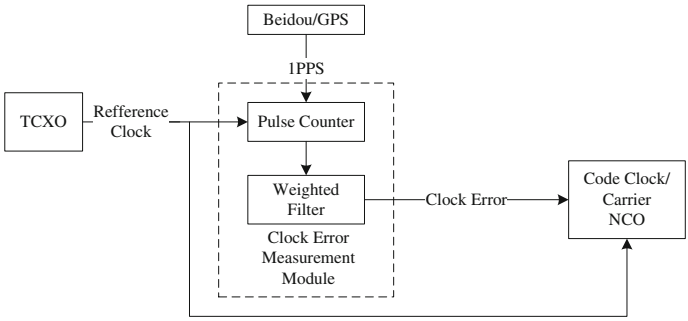

Fig. 9 Consisting of clock error correction

$$\hat{x} = \sum_{i=0}^{n-1} W_i(n) x_{n-i} \tag{9}$$

x_{n-i}, 1PPS count number; $W_i(n)$, weight coefficient; n, length of measurement window, the longer the length, the higher the precision.

4 Conclusions

In this study, a new spread spectrum code phase and carrier frequency correction method based on Beidou/GPS timing is proposed. For the key of spread spectrum signal acquisition: code phase and carrier frequency offset, network-wide time synchronization system is constructed and to correct from three aspects based on Beidou/GPS timing: code phase error, carrier frequency offset, and clock error. The acquisition of spread spectrum signal is greatly accelerated due to the correction of code phase and carrier frequency. The method of this paper is simple with low cost, not only for satellite spread spectrum communication system, also can be applied to other ground mobile or fixed station communications.

References

1. Cui J, Shi H et al (2008) The transmission link of CAPS navigation and communication system. Sci China Ser G Phys Mech Astron 38(12):402–411. doi: 10.1007/s11433-009-0062-9
2. Tsui JBY (2008) Fundamentals of global positioning system receivers a software approach, 2nd edn. (trans: Chen J et al). Publishing House of Electronics Industry, Beijing
3. Ricai T (2007) Spread spectrum communication. Tsinghua University Press, Beijing
4. Chu Y (2012) Application of time synchronization equipment in mobile communication network. Mod Transm 4:58–62. doi:10.3969/j.issn.1673-5137.2012.08.004

5. Hwa Create Corporation Ltd. (2013) HM-1103C navigation/timing module data sheet V1.1. Beijing
6. Kaplan ED, Hegarty CJ (2007) Understanding GPS principles and applications, 2nd edn. (trans: Kou Y). Publishing House of Electronics Industry, Beijing
7. Ma X, Kong W, Sun H (2011) Design of a frequency calibration system based on GPS disciplined rubidium clock. Telecommun Eng 51(10):109–112. doi:10.3969/j.issn.1001-893x.2011.10.022
8. Shan Q, Yang J (2009) Review of satellite disciplined clock system. J Test Meas Technol 23(5):396–401. doi:10.3969/j.issn.1671-7449.2009.05.005
9. O'Leary P, Maloberti F (1991) A direct-digital synthesizer with improved spectral performance. Commun IEEE Trans 39(7):1046–1048. doi:10.1109/26.87209
10. Zhao Y (2001) Arithmetic mean method and weighting mean method of digital filter. Instrum Technol 4:41–44. doi:10.3969/j.issn.1006-2394.2001.04.017

The Effect of GNSS Sites Distribution on TEC Derivation

Xiaolan Wang, Guanyi Ma, Qingtao Wan, Jinghua Li, Jiangtao Fan and Jie Zhang

Abstract With worldwide increased Global Navigation Satellite System (GNSS) receivers, it is possible to obtain the ionospheric total electron content (TEC) and hence monitor the ionosphere with GNSS. Using a thin layer assumption of the ionosphere and dual-frequency Global Positioning System (GPS) observations from 16 geomagnetically quiet days in four seasons of 2006, this paper adopts the spherical harmonic model to fit TEC and investigates the effects of two network constitutions on global TEC derivation, one with 275 GPS receivers and the other with 125 GPS receivers. The results show that the data can be well fitted for both network constitutions. The derived TECs are consistent with each other for four seasons. This is especially true for TECs at low- and mid-latitude. The derived satellite and receiver biases are stable during the year. The standard deviation of the satellite and the receiver biases are less than 0.5 and 3 ns, respectively.

Keywords GPS · TEC · Sites distribution · Spherical harmonic model

1 Introduction

As a dispersive medium, the ionosphere can cause a time delay to transionospheric radio waves, which is proportional to the total electron content (TEC) along the ray path of radio wave propagation. TEC is one of the important parameters of studying the ionospheric characteristics, and the measurement of TEC is an important task for ionospheric corrections in transionospheric radio system [1]. With the extensive development and application of GNSS, the ionospheric TEC has been measured with GNSS receivers economically and effectively. The derived TEC has been

X. Wang (✉) · G. Ma · Q. Wan · J. Li · J. Fan · J. Zhang
National Astronomical Observatories, Chinese Academy of Sciences, Beijing, China
e-mail: xlwang@nao.cas.cn

X. Wang
University of Chinese Academy of Sciences, Beijing, China

J. Sun et al. (eds.), *China Satellite Navigation Conference (CSNC) 2016 Proceedings: Volume I*, Lecture Notes in Electrical Engineering 388,
DOI 10.1007/978-981-10-0934-1_3

used to construct models for improving the positioning precision of GNSS user and monitor the ionospheric activity for space weather.

Since the civilian use of Global Positioning System (GPS) and GPS receivers being set up worldwide, TEC derivation methods have been studied continuously [1–12]. Center for Orbit Determination in Europe (CODE), the Jet Propulsion Laboratory (JPL), the European Space Agency (ESA), Canadian Energy, Mines and Resources Center (EMR), Polytechnic University of Catalonia in Spain (UPC), National Institute of Information and Communication Technology in Japan (NICT), and institute of geology and geophysics, Chinese academy of sciences (IGGCAS) have completed the relevant study on the algorithm of the ionosphere TEC products and released the analysis results. In the early times, the ionosphere was observed with a single GPS receiver, the instrumental biases and the TEC were assessed by representing the TEC as a polynomial of latitude and longitude [2]. Later using observation data from several GPS receivers, the TEC and instrumental biases were derived by random walk stochastic process and solved by Kalman filter method [3]. With the global network of over 100 GPS receivers, JPL models the vertical TEC to bi-cubic splines on a spherical of 2.5° by 5.0° latitude and longitude, then by Kalman filter method to solve the TEC and instrumental biases [4]. Using around 300 GPS receivers selected homogeneously from GEONET, and assuming that the TEC is identical at any point within 2° by 2° grid block, the TEC over Japan and instrumental biases were determined least-squares fitting method [7]. However, instrumental biases exist in the hardware of the GPS satellite and receiver which affects the accuracy of the TEC estimation greatly. For accurate TEC derivation, satellite and receiver biases should be removed properly.

Based on a thin layer assumption of the ionosphere and the spherical harmonic model, this paper adopts the algorithm spherical harmonic model to derive TEC for two network constitutions, one with 275 GPS receivers and the other with 125 GPS receivers. With the observation data selected from 16 geomagnetically quiet days in 2006, 5–8 March, 23–26 June, 10–13 September, and 26–29 December, covering a period of 10 months, we analyze the effect of the sites distribution on TEC derivation.

2 Transionospheric Radio Propagation

A GPS receiver measures two pseudoranges (P_1 and P_2) and two carrier phases (L_1 and L_2) corresponding to two signals at 1575.42 MHz (referred to as f_1) and 1227.6 MHz (referred to as f_2). The slant TEC along the ray path can be calculated as

$$\mathrm{STEC}_p = \frac{2(f_1 f_2)^2}{k(f_1^2 - f_2^2)}(P_2 - P_1) \tag{1}$$

$$\mathrm{STEC}_l = \frac{2(f_1 f_2)^2}{k(f_1^2 - f_2^2)}(L_1\lambda_1 - L_2\lambda_2) \tag{2}$$

where $k = 80.62\ \mathrm{m}^3/\mathrm{s}^2$, λ_1 and λ_2 are the wavelengths corresponding to f_1 and f_2, respectively. To reduce the effects of the pseudorange error on TEC, a baseline or offset between STEC_p and STEC_l can be used to obtain an absolute slant TEC with higher precision [7]

$$B_{rs} = \frac{\sum_{i=1}^{N}(\mathrm{STEC}_{p_i} - \mathrm{STEC}_{l_i})\sin^2\alpha_i}{\sum_{i=1}^{N}\sin^2\alpha_i} \tag{3}$$

$$\mathrm{STEC} = \mathrm{STEC}_l + B_{rs} \tag{4}$$

where α_i is the elevation of the satellite. The square sine of the elevation $\sin^2\alpha_i$ is included as a weighting factor, as the pseudorange with low elevation apt to be affected by the multipath effect and the reliability decreases.

When studying the ionosphere, the vertical TEC (refers to TEC hereafter) is generally used, which refers to the TEC along the path that passes through the earth center and cross the ionosphere perpendicularly. To convert the STEC to TEC, we assume the ionosphere as a single thin layer at height h above the earth as shown in Fig. 1.

The intersection of the slant path from the satellite S to the receiver R through the ionosphere is referred to as piercing point P. The zenith angle χ is expressed as the following:

$$\chi = \arcsin\left(\frac{R_e \cdot \cos\alpha}{R_e + h}\right) \tag{5}$$

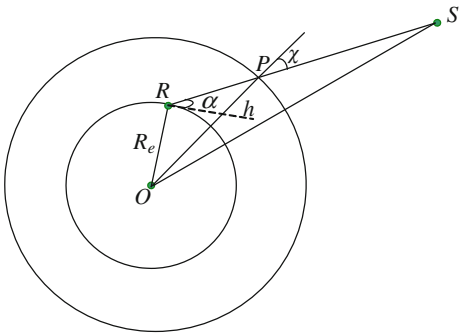

Fig. 1 Geometry of single layer model

where R_e is the mean radius of the Earth. The vertical TEC at the piercing point can be obtained

$$\mathrm{VTEC} = (\mathrm{STEC} - b_s - b_r) \cdot \cos\chi \tag{6}$$

with b_s and b_r corresponding to the satellite and receiver biases, respectively. The $\cos\chi$ is the oblique-to-zenithal factor or the mapping function. With the spherical harmonic model, the vertical TEC can be expressed as follows [13]

$$\mathrm{VTEC}(\varphi,\lambda) = \sum_{n=0}^{n_{\max}} \sum_{m=0}^{n} \tilde{P}_{nm}(\sin\varphi)(\tilde{C}_{nm}(\cos m\lambda) + \tilde{S}_{nm}(\sin\, m\lambda)) \tag{7}$$

where φ and λ are the geocentric latitude and the sun-fixed longitude of the ionosphere pierce point, $n_{\max}$ is the max order of the spherical harmonic, $\tilde{P}_{nm}(\sin\varphi) = \mathrm{MC}(n,m)P_{nm}(\sin\varphi)$ is the normalized Legendre polynomials, $\mathrm{MC}(n,m)$ is the normalization function, $\tilde{C}_{nm}$ and $\tilde{S}_{nm}$ are the coefficient of the spherical harmonic.

3 TEC Derivation

For the line of sight from satellite j to receiver k piercing through the ionosphere at time t, referring to Eq. 7 and putting the unknowns in the left side, we can write the following equation:

$$\sec\chi_{jk}\,\mathrm{VTEC}_{jk} + b_{sj} + b_{rk} = \mathrm{STEC}_{jk} \tag{8}$$

Using Eq. 7 we can obtained the following:

$$\begin{cases} Y_{n0} = \tilde{P}_{n0}(\sin\varphi) \\ Y_{nmc} = \tilde{P}_{nm}(\sin\varphi)C_{nm}(\cos m\lambda) = \mathrm{MC}_{nm}C_{nm}P_{nm}(\sin\varphi)(\cos m\lambda) \\ Y_{nms} = \tilde{P}_{nm}(\sin\varphi)S_{nm}(\sin m\lambda) = \mathrm{MC}_{nm}S_{nm}P_{nm}(\sin\varphi)(\sin m\lambda) \end{cases} \tag{9}$$

Finally, VTEC can expressed as,

$$\mathrm{VTEC} = [Y_{00}, Y_{10}, Y_{11c}, Y_{11s}, Y_{20}, Y_{21c}, Y_{21s}, \ldots] \tag{10}$$

In this paper the order of spherical harmonics expansion is taken to be $n_{\max} = 8$. For J satellites and K receivers, we can have a matrix form of equations from Eq. 8,

$$H \cdot \begin{bmatrix} E \\ B \end{bmatrix} = \mathrm{STEC} \tag{11}$$

where $E = [e_{00}, e_{10}, e_{11c}, e_{11s}, \ldots, e_{87c}, e_{87s}, e_{88c}, e_{88s}]$ is the coefficient of the spherical harmonic, $B = [b_{s1}, \ldots, b_{sJ}, b_{r1}, \ldots, b_{rK}]$ is the biases of satellites and receivers $H = \begin{bmatrix} \vdots & \vdots & \cdots & \cdots & \cdots & \cdots & \cdots \\ \sec\chi_{jk} P_{nm}(\sin\varphi)(\sin m\lambda) & \sec\chi_{jk} P_{nm}(\sin\varphi)(\sin m\lambda) & 0 & 1 & 0 & 1 & 0 \\ \vdots & \vdots & \cdots & \cdots & \cdots & \cdots & \cdots \end{bmatrix}$ is the matrix of coefficients with a dimension of $M \times N (N = 81 + J + K,\ M > N)$.

With a least-squares fitting technique, the solution to the set of equations can be obtained by the singular value decomposition (SVD), and the matrix of coefficients can be decomposed as the following [14]:

$$H = [U] \cdot \begin{bmatrix} \omega_1 & & & \\ & \omega_2 & & \\ & & \cdots & \\ & & & \omega_N \end{bmatrix} \cdot [V^T] \tag{12}$$

where U and V are orthogonal matrix, the dimension is $M \times M$ and $N \times N$, respectively, and $\omega_n (n = 1, \ldots, N)$ is the singular values of a diagonal matrix. Then the least-squares solution of Eq. 11 can be computed,

$$\begin{bmatrix} E \\ B \end{bmatrix} = [V] \cdot [\mathrm{diag}(1/\omega_n)] \cdot \left[U^T\right] \cdot \begin{bmatrix} \vdots \\ \mathrm{STEC}_{jk} \\ \vdots \end{bmatrix} \tag{13}$$

Because it is not possible to determine unambiguously all of the satellites and receiver biases absolutely, one of them should be set to be 0, as a reference. Here, the reference is taken to be the satellite with pseudorange number of 1. Subsequently, the spherical harmonic coefficients, satellite biases, and receiver biases can be obtained by solving Eq. 13. Then, VTEC is computed with Eq. 7.

4 Network Constitution and Results

We use two network constitutions to investigate the effect of site distribution TEC derivation. One network constitution consists of 275 GPS receivers of International GNSS Service (IGS), the other one selects 125 receivers from IGS. The site distribution of the two network constitutions are shown in Fig. 2.

Latitudinal distribution of the sites is shown in Fig. 3, where the horizontal axis refers to the sites number, the vertical axis shows latitude ranges, HN: 60°N–90°N, MN: 30°N–60°N, LN: 0°N–30°N, HS: 60°S–90°S, MS: 30°S–60°S, LS: 0°S–30°S. As seen in Fig. 3, a main difference of 115 receivers for the two network constitutions happens in MN area. This indicates that the GPS receivers are mostly dense in northern middle latitudes.

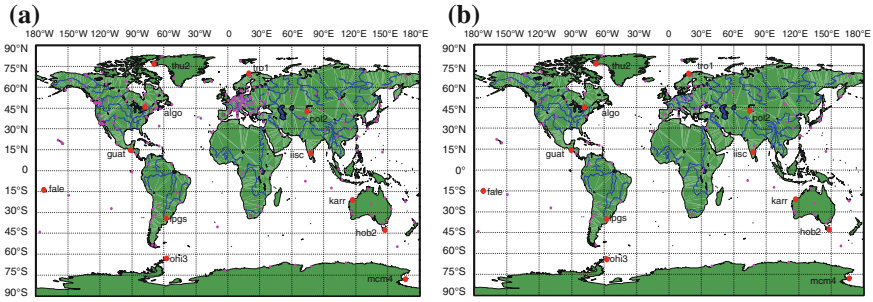

Fig. 2 GPS sites map (*red dots* are the location of selected 12 sites distribution, *pink dots* are the location of the rest of the sites distribution). **a** 275 GPS sites map, **b** 125 GPS sites map (Color figure online)

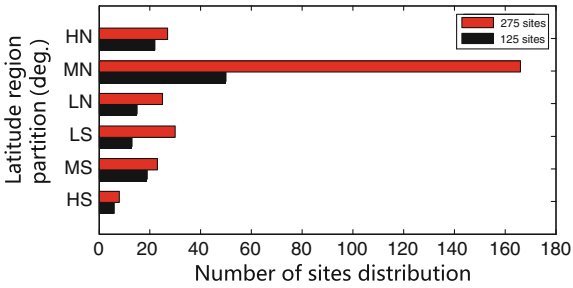

Fig. 3 Distribution of the number of sites with latitude changes (Color figure online)

Table 1 Geographic coordinates of the 12 GPS sites

Site	Latitude(°)	Longitude(°)	Site	Latitude(°)	Longitude(°)
THU2	76.54°N	68.82°W	FALE	13.83°S	171.99°W
ALGO	45.96°N	78.07°W	LPGS	34.91°S	57.93°W
GUAT	14.59°N	90.52°W	OHI3	63.32°S	57.90°W
IISC	13.02°N	77.57°E	KARR	20.98°S	117.09°E
POL2	42.68°N	74.69°E	HOB2	42.80°S	147.44°E
TRO1	69.66°N	18.94°E	MCM4	77.84°S	166.67°E

In order to examine the results and make comparison, we also selected 12 sites whose locations are listed in Table 1. With the observation data selected from 16 geomagnetically quiet days in 2006, 5–8 March, 23–26 June, 10–13 September, and 26–29 December, covering a period of 10 months, we analyze the effect of the sites distribution on TEC derivation. Here, the ionospheric height is taken to be 450 km and the time resolution of GPS observation data is 15 min.

It consists of two processes for TEC derivation. One process is to read and filter the observation data, and then constitute equations. The other process is to solve the equations. The calculating time of derived TEC from 275 GPS receivers is about 1 h 45 min 56 s and 7 min 44 s, and it is 41 min 55 s and 2 min 58 s from 125 GPS receivers. There is 1 h 8 min 47 s time difference with the two network constitutions.

4.1 Derived TEC

Figure 4 shows TEC maps with the two network constitutions at 6:00 UT on March 8, June 23, September 13, and December 29, the left column corresponds to 275 receivers, the right column is from 125 receivers. Not much difference can be seen from the two network constitutions for four seasons TEC peaks at low mid-latitude. Meanwhile, the TEC value is larger in the spring and autumn, and it is smaller in the summer and winter. The differences between maximum TECs are 2.24 TECU, 0.95 TECU, 0.15 TECU, and 0.84 TECU for the four seasons, respectively. The differences between locations where the maximum TECs occur are very similar to one another and it is less than 2° in latitude and not more than 10° in longitude. Meanwhile, the derived TEC are compared to those obtained from CODE, the results indicate that the derived TEC in 2006 are in agreement with those obtained from CODE.

Figure 5 shows derived TEC in 16 days for the 12 observation stations in Table 1, where the red curves represent the derived TEC from 275 sites, and black curves represent the derived TEC from 125 sites. As seen in the figure, the derived TEC tends to be consistent with each other and the TEC peaks at the same time every day. This is especially true for TECs over middle and low latitude sites. The TECs at high latitude are much noisy. Though why this is so is not the research topic of this paper, we should point out that the ionosphere is much more variable at high latitudes than that at middle and low latitudes.

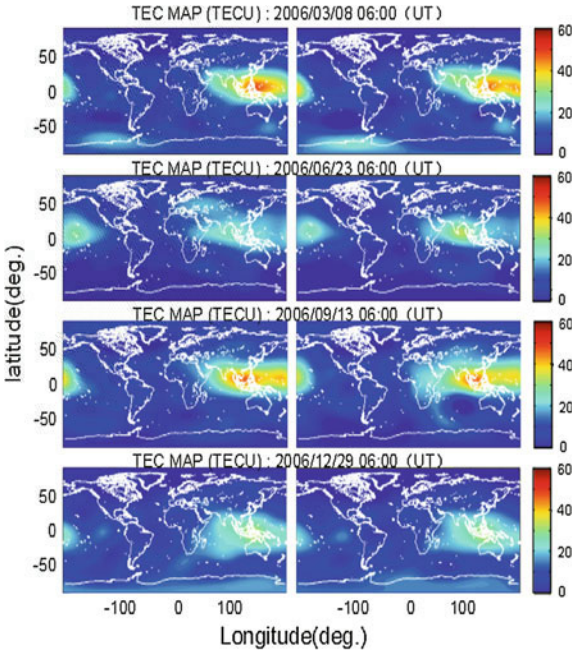

Fig. 4 The TEC maps at 6:00 UT (Color figure online)

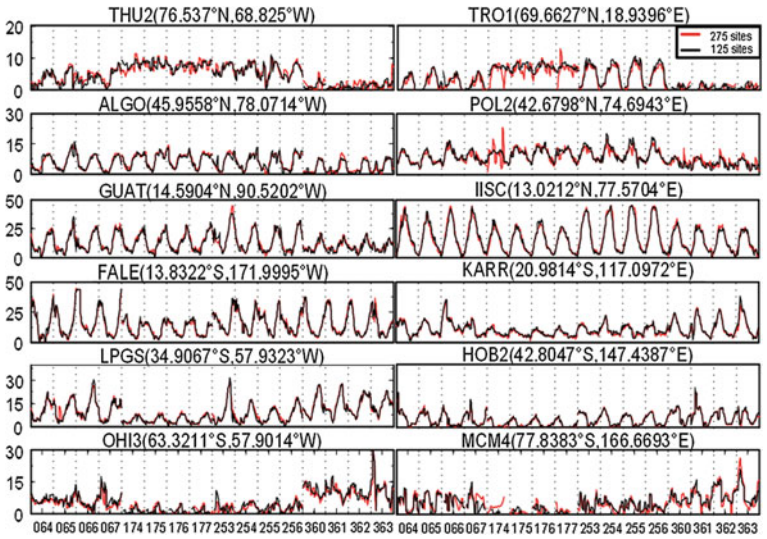

Fig. 5 TEC contrast figure of 12 sites (Color figure online)

4.2 The Satellites Biases

Figure 6 shows the comparison of estimated satellites biases for the 16 days from the two network constitutions which one is 275 sites and another is 125 sites, where the horizontal axis represents the satellites biases derived from 275 sites and the vertical axis represents the satellites biases derived from 125 sites. As can be seen, the difference of satellites biases from the two network constitutions is almost unanimously.

Figure 7 shows the 31 GPS satellites biases for the 16 days derived from 125 GPS sites. Vertical dashed lines divide non-consecutive days. As seen in the figure, two satellites (PRN 12 and PRN 31) were observed in 4 days in winter (360–363), and were not observed in the remaining 12 days. On the days 176 and 177, the bias

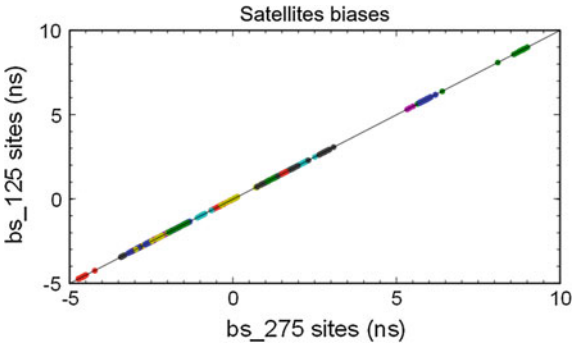

Fig. 6 Satellites biases contrast figure

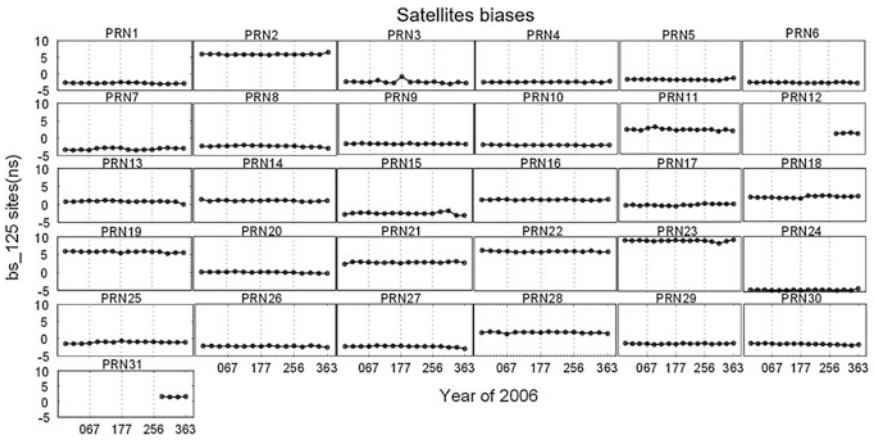

Fig. 7 Satellites biases derived from 125 GPS sites

of PRN3 shows a large variation. The difference is 1.9 ns between the two days. The remaining satellites biases show small changes in 16 days. For the 16 days, the standard deviation of 31 GPS satellites biases ranges 0.0796–0.4881 ns.

4.3 The Receivers Biases

Figure 8 shows the comparison of receivers biases derived from 275 sites and 125 sites, where the horizontal axis represents the receivers biases derived from 275 sites and the vertical axis represents the receivers biases derived from 125 sites. As can be seen, the difference of receivers biases with different network constitution is extremely close and not big changed.

Figure 9 shows the biases of 12 receivers from Table 1 in 16 days derived from 125 GPS sites. Vertical dashed lines divide non-consecutive days. Shown in the

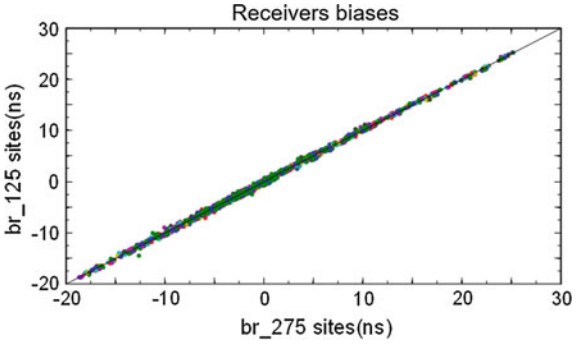

Fig. 8 Receivers biases contrast figure

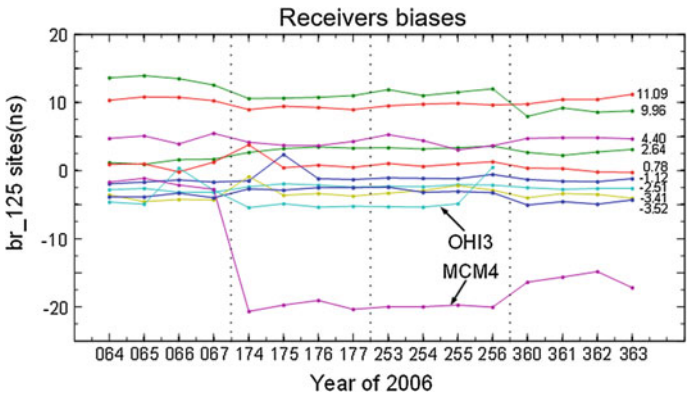

Fig. 9 Receivers biases derived from 125 GPS sites (Color figure online)

right are the mean of the receiver biases. As seen in the figure, the types of the 12 receivers are ASHTECH Z18, TRIMBLE 4000SSI, ASHTECH Z-XII3, AOA BENCHMARK ACT. The different hardware is likely to cause the different biases. For example, the difference can be achieved 10.3 ns between the types of AOA BENCHMARK ACT and ASHTECH Z-XII3. Except three receivers, MCM4, OHI3, FALE, the remaining nine receivers are relatively stable for different seasons. For the 16 days covering 10 months, the standard deviation of the receiver biases ranges from 0.3673 to 0.9759 ns. As for the large variation of MCM4, we found that its receiver was in type AOA SNR-12 ACT for spring, whose standard deviation is 0.6953 ns, and it was changed to ASHTECH Z-XII3 in summer, autumn, and winter, whose standard deviation is 2.053 ns. Therefore, the receiver biases curve of MCM4 has a greater change. The receiver biases of OHI3 station do not get on the days of 360–363 of 2006, the reason is, the data of IHO3 station are removed when the observation data is preprocessing. For the same reason, the receiver biases curve of FALE station is not plotted in Fig. 9.

5 Conclusion

Using a thin layer assumption of the ionosphere and dual-frequency GPS observations from 16 geomagnetically quiet days in four seasons of 2006, this paper adopts the spherical harmonic model to fit TEC and investigates the effects of two network constitutions on global TEC derivation, one with 275 GPS receivers and the other with 125 GPS receivers. The results show that the data can be well fitted for both network constitutions. The derived TECs are consistent with each other for four seasons. This is especially true for TECs at low- and mid-latitude. The TECs at high latitude are much noisy and lack of consistency. This can be attributed to that the ionosphere is much more variable at high latitudes than that at middle and low

latitudes. The derived satellite and receiver biases are stable during the year. The standard deviation of the satellite and the receiver biases are less than 0.5 and 3 ns, respectively. Concerning the processing time of TEC derivation, the difference is 1 h 8 min 47 s between the two network constitutions. We can conclude that it can not only derive TEC effectively but also reduce the calculating time by selecting the appropriate network constitution. Further work should be done on finding a practical method to constitute GPS receivers network.

Acknowledgments This work is supported by the National Natural Science Foundation of China (Grant Nos. 11473045, 11403045).

References

1. Lanyi GE, Roth T (1988) A comparison of mapped and measured total ionospheric electron content using global positioning system and beacon satellite observations. Radio Sci 23(4):483–492
2. Coco DS, Coker C, Dahlke SR, Clynch JR (1991) Variability of GPS satellite differential group delay biases. IEEE Trans Aerosp Electron Sys 27(6):931–938
3. Sardon E, Rius A, Zarraoa N (1994) Estimation of the transmitter and receiver differential biases and the ionospheric total electron content from global positioning system observations. Radio Sci 29(3):577–586
4. Mannucci A, Wilson B, Yuan D, Ho C, Lindqwister U, Runge T (1998) A global mapping technique for GPS-derived ionospheric total electron content measurements. Radio Sci 33(3):565–582
5. Iijima B, Harris I, Ho C, Lindqwister U, Mannucci A, Pi X, Reyes M, Sparks L, Wilson B (1999) Automated daily process for global ionospheric total electron content maps and satellite ocean altimeter ionospheric calibration based on global positioning system data. J Atmos Sol Terr Phys 61(16):1205–1218
6. Rideout W, Coster A (2006) Automated GPS processing for global total electron content data. GPS Solut 10(3):219–228
7. Ma G, Maruyama T (2003) Derivation of TEC and estimation of instrumental biases from GEONET in Japan. Ann Geophys 21:2083–2093
8. Li Z, Yuan Y, Li H, Ou J, Huo X (2012) Two-step method for the determination of the differential code biases of COMPASS satellites. J Geod. doi:10.1007/s00190-012-0565-4
9. Gao W, Ma G, Chen Y, Shen H, Li J, Huang W, Li Z (2008) Derivation of GPS-TEC and instrumentao biases in the equatorial anomaly region. Chin J Space Sci 28(6):541–546
10. Ma G, Gao W, Li J, Chen Y, Shen H (2014) Estimation of GPS instrumental biases from small scale network. Adv Space Res 54:871–882
11. Kaplan ED, Hegarty CJ (2006) Understanding GPS: principles and applications. Artech House Publishers, London
12. Liu J, Chen J, Zhang Y, Li S, Ge M (1999) WADGPS principle and method. Surveying and mapping Press, Wuhan
13. http://gpspp.sakura.ne.jp/, Cited 20 Mar 2015
14. Zhang X (2004) Matrix analysis and applications. Tsinghua University Press, Beijing

GNSS-R Aircraft Flight Test Based on Digital Beam Forming

Kangning Zhang, Fenghui Li, Xingguo Li, Linfei He, Qijia Dong, Wenliang Zhao and Fuzhan Yue

Abstract The technology can be used to measure the wind and the height of the sea based on the GNSS-R, It can be complementary to the other advantages of sea measurements, has more advantages than other methods when it can be used to constitute constellation. When to deal with the environments of the sea surface, only need is to install the receiver, so compared to traditional means of remote sensing, GNSS-R technology reduce costs, weight, and the power, at the same time, the technology can improve the resolution and accuracy, It can be used to the new way at remote sensing. This paper designs a new GNSS-R receiver based on the Digital beam forming (DBF), the receiver through the dbf to synthesis the receive signal. The receiver has 31 dbf channels, so it can complete the synthesis a plurality of different direction's signal at the same time. In order to effectively improve the detection area, the receiver can achieve the angle scanning between the fixed angle and the dynamic angle. In order to test the receiver, we did an experiment by using the plane on November 3, 2015 at Bohai Bay, flying height about 1200 meters, in the experiment, we successfully captured the reflected signals at the high altitude (1.2 km) dynamic scenes, after that we got the delay-doppler mapping through to deal with the reflected signals. By calculating the phase difference between the reflection channel's DDM and direct access, we got the high information of the receiver, after that we compared the high information that can be got through the receiver, the answer showed that the deviation is less than 4 m.

Keywords Delay-doppler mapping · Digital beam forming · Sea surface altimetry

K. Zhang (✉) · F. Li · X. Li · L. He · Q. Dong · W. Zhao · F. Yue
Space Star Technology Co., Ltd., Beijing 100086, China
e-mail: ning_zhang_139@163.com

J. Sun et al. (eds.), *China Satellite Navigation Conference (CSNC) 2016 Proceedings: Volume I*, Lecture Notes in Electrical Engineering 388,
DOI 10.1007/978-981-10-0934-1_4

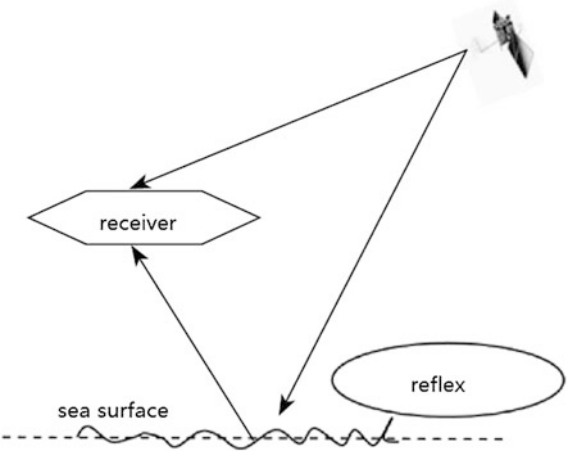

Fig. 1 Detective of the GNSS-R

1 Introduction

It is the important physical parameter of the Marine Science Subject based on the high level of the sea, wave height, and wind field of the sea surface [1]. As a new type of passive detection technology, The GNSS-R technology has developed rapidly. GNSS-R technology does not require additional signal source transmitter, Because GNSS-R only used the navigation satellite signal. As shown in Fig. 1, GNSS-R receiver at the same time receives the navigation satellite direct signal, but also received from the sea scattered signal. The reflection signals from the sea surface carry the characteristics of the sea surface, and the sea surface features are mainly reflected by the reflection wave, polarization characteristics, amplitude, phase, frequency, and other parameters. So, the physical characteristics of the reflecting surface can be effectively reflected by the receiving and processing of the reflected signal. This paper designs a new GNSS-R receiver based on the digital beam forming, and using the receiver did an experiment by using the plane on November 3, 2015 at Bohai Bay. In the experiment, the GNSS-R receiver captures the reflected signal from the sea, and generated the DDM. The experiments get the receiver's height information by calculating the phase difference between the reflection channel and the direct channel.

2 The Principle of GNSS-R

It is an important direction in the current GNSS-R research to measure the height of the receiver by using the GPS sea surface reflection signal. The basic principle is to use the time difference between the sea surface reflection signal and the direct signal to calculate the different distance. So, the value can help the receiver to get the

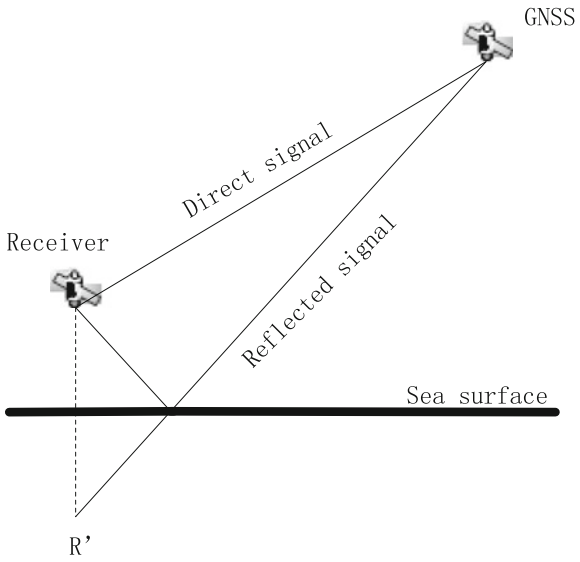

Fig. 2 Altimetry principle of GNSS-R

height from the sea surface to the receiver [2]. The principle is as shown in Fig. 2. In this diagram, R stands for the position of the receiver, R′ stands for the position of the mirror image of receiver. As shown in Fig. 2, we can get the geometric relationships as $\Delta\rho = 2h\sin(\varepsilon)$.

The flow chart in Fig. 3 demonstrates how to measure the height from the sea surface to the receiver.

The specific process is as follows:

1. First got the measured data, including L1 carrier, CA code data, receiver and satellite position, and speed information.
2. According to the observation time, or the position and velocity information of the receiver and the satellite, calculated the position of the specular reflection point and reflection angle.
3. Using carrier and code data modified the delay due to the ionosphere.
4. Acquisition mode or real-time atmospheric refractive index profile, calculated neutral atmospheric additional delay.
5. By analyzing the change of the wave front gradient, the position of the specular reflection point is determined, according to the answer, the delay between the reflection wave and the direct wave is calculated, at last the sea surface height can be retrieved after deducting the additional delay.

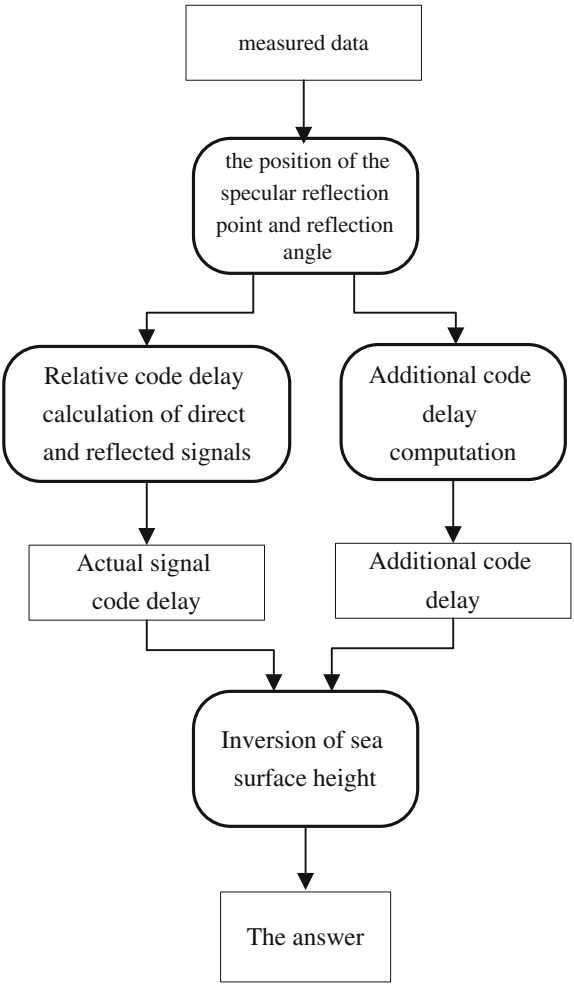

Fig. 3 Flow chart of the way to get the high of sea surface

3 The Composition of GNSS-R Detection System Based on dbf

3.1 System Components of the GNSS-R Receiver

The GNSS-R receiver system is made of the navigation and positioning antenna, the reflector antenna, GNSS-R receiver and the data logger instrument. As shown in Fig. 4.

The navigation and positioning antenna mounted on the top of the airplane, in order to receive the multiple frequency point direct signal from GPS and BD2 navigation constellation. Output the RF signal to GNSS-R receiver. The reflector

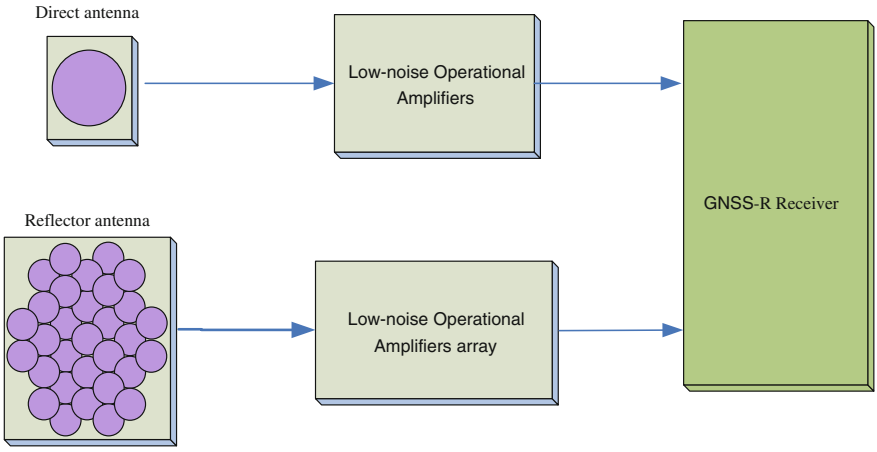

Fig. 4 System components of the GNSS-R receiver

antenna mounted on the bottom of the airplane, in order to receive the signal from the ocean reflection signal, Output the RF signal to the Low-noise Operational Amplifiers array. After that, the amplified signal output can be sent to the radio frequency unit of the GNSS-R receiver. Sent to the GNSS-R receiver's navigation signal, In the radio frequency processing channel, the signal is amplified, filtered, and downconvertedn, after that the analog signal is formed. In the baseband processing module, the receiver using the digital correlates to complete the digital intermediate frequency signal, gets the original measurement and navigation message. After that, the DSP deals with the information to obtain the navigation positioning information and ephemeris and almanac information and reflection signal.

3.2 Digital Beam Forming

The principles of digital beam synthesis [3], as shown in Fig. 5,

$d_m = -(x_m \cdot \cos\varphi_m + y_m \cdot \sin\varphi_m) \cdot \sin\theta_m$, x_m is the x-axis coordinate value of the m antennas, y_m is the y-axis coordinate value of the m antennas, φ_m is the azimuth angle of the m antennas, and θ_m is the pitch angle of the m antennas. So, the array response vector is

$$a(\theta, \varphi) = [1, \mathrm{e}^{-j\xi_2}, \mathrm{e}^{-j\xi_3}, \ldots, \mathrm{e}^{-j\xi_{31}}]^{\mathrm{T}}$$

Hypothesis that the first antennas receive the signal that can be credited to $x_1(n) = s(n)$, So, all the antennas received signal can be written as:

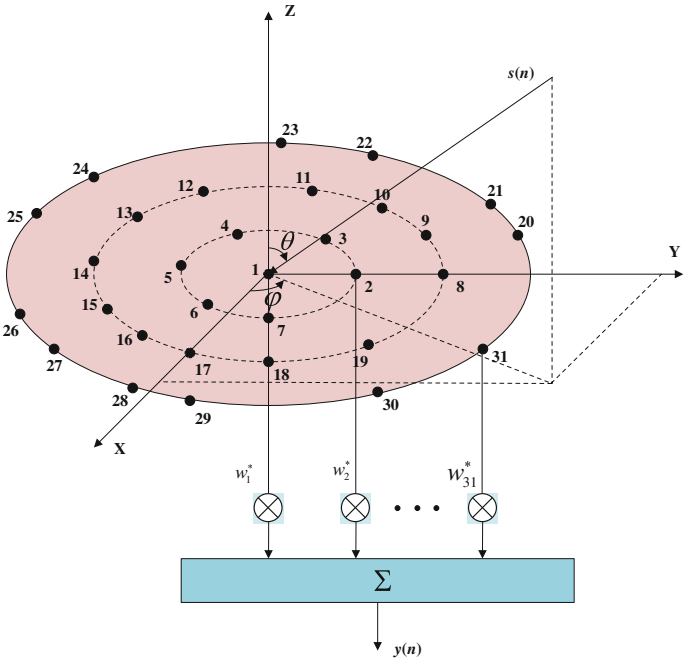

Fig. 5 The theory of the dbf

$$x(n) = [x_1(n), x_2(n), \ldots, x_{31}(n)]^{\mathrm{T}} = a(\theta, \varphi)s(n)$$

After that, the dbf output is $y(n) = w^H x(n) = w^H a(\theta, \varphi)s(n)$.

3.3 Anechoic Chamber Test

In order to test the results of the dbf, we put all the equipment into the anechoic chamber, tests the dbf effect in the real environment. The schematic diagram can be shown in Fig. 6. In the anechoic chamber, we were suspending the reflector antenna. In order to reduce the lost, the transmitting antenna selects the linear polarization antenna, and the 1575.42 MHz carrier signal is transmitted from the transmitting antenna. After treatment, the actual effect is analyzed.

Through the experiment can be seen the phase difference between the signals before and after calibration comparison which is obvious. Status contrast between before and after calibration is as shown in Fig. 7, and the phase difference between the signals before and after calibration comparison is as shown in Fig. 8.

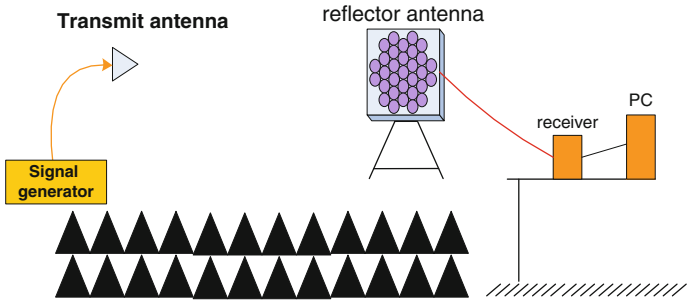

Fig. 6 Schematic diagram of anechoic chamber test

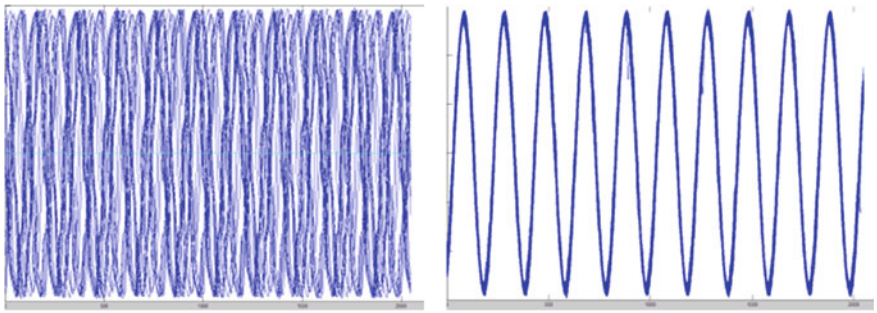

Fig. 7 Status contrast between before and after calibration

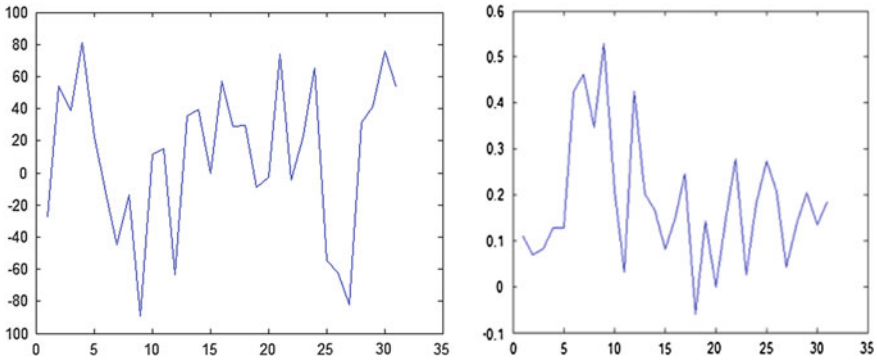

Fig. 8 The phase difference between the signals before and after calibration comparison

4 Flight Test Verification

4.1 Flight Equipment

In the equipment, we use the plane as shown in Fig. 9.

Equipment connection diagram is as shown in Fig. 10. Positioning antenna installed on top of the plane receives the signal from the satellite. The reflector antenna is mounted on the bottom of the airplane, in order to receive the signal from the ocean reflection signal. Optoelectronic pod mounted on the bottom of the airplane too needs to close the reflector antenna. The receiver completes the signal processing between the direct and reflected signals. The direct signal is used to the position calculation, and the reflector channel mainly used to complete the dbf.

The GPS navigation satellite distribution map in the area of flight test work is as shown in Fig. 11.

The collected data are analyzed, combined with the flight path map of the aircraft, the aircraft's flight attitude information (course), and the GPS navigation satellite distribution map we can get the status of the captured satellite.

Fig. 9 The real image of the plane

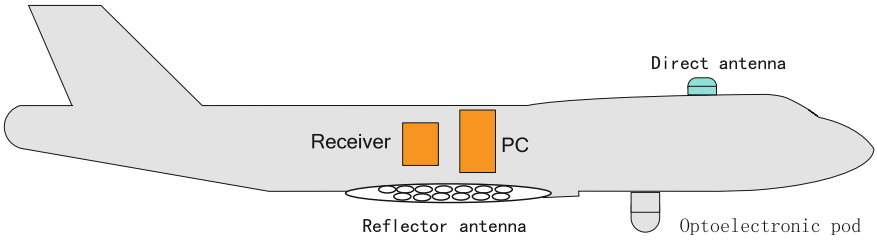

Fig. 10 Equipment connection diagram

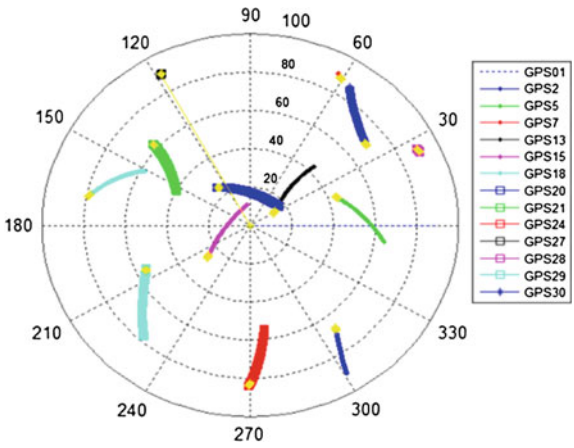

Fig. 11 Prediction of GPS satellites position (Color figure online)

4.2 Experimental Study

Through the analysis of the test data can be judged that the receiver gets the ocean reflection signal from the 13 satellite. After processing, the DDM shown is shown in Figs. 12, 13, 14.

According to the measure, the system gets the high information, compared with that of the receiver as shown in Fig. 15. The measurement error is less than 4 m.

This paper detailed introduced the receiver's work principle based on digital beam forming, calibration mode, and the height measurement theory. Experiment

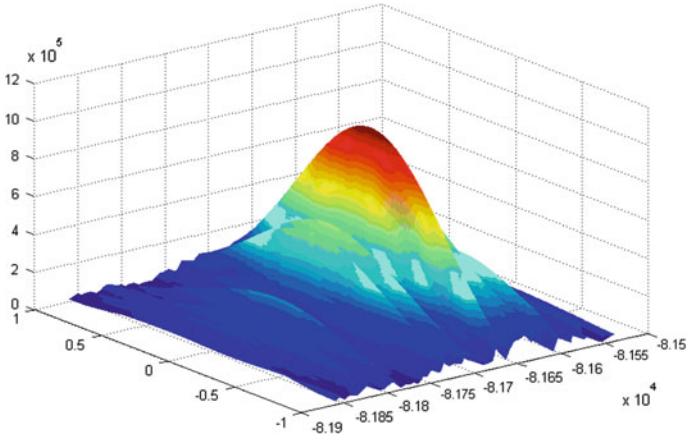

Fig. 12 The DDM of the satellite 13

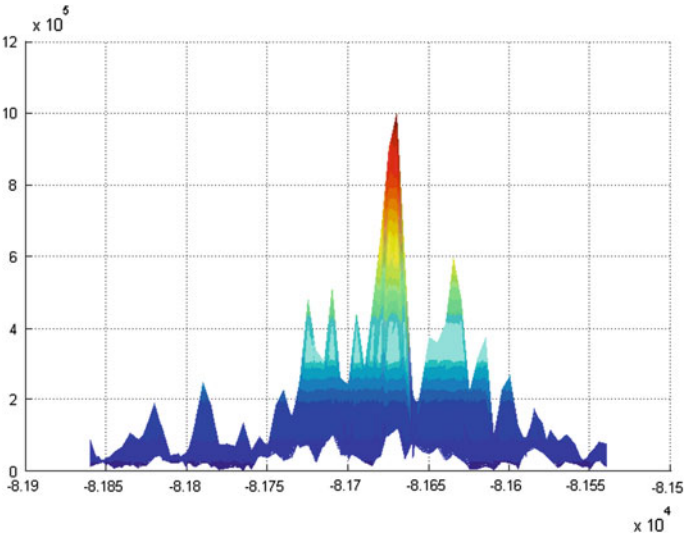

Fig. 13 The doppler mapping of the satellite 13

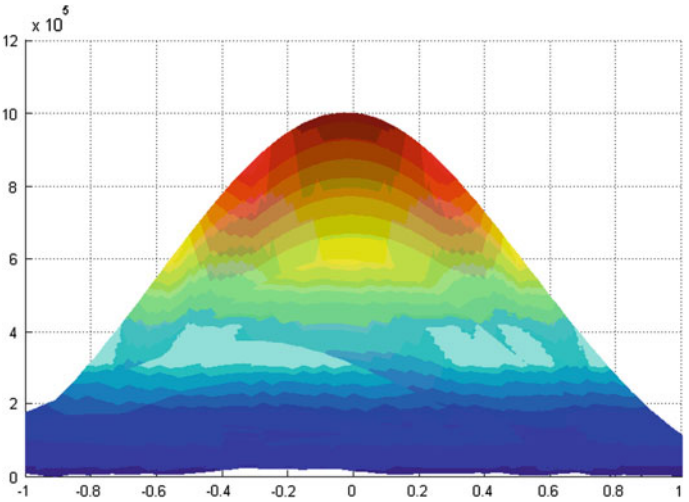

Fig.. 14 The delay mapping of the satellite 13

was done by using the plane on November 3, 2015 at Bohai Bay. By analyzing the data of the flight test, got the DDM map of the ocean reflected signal; go the high information. The measurement error is less than 4 m.

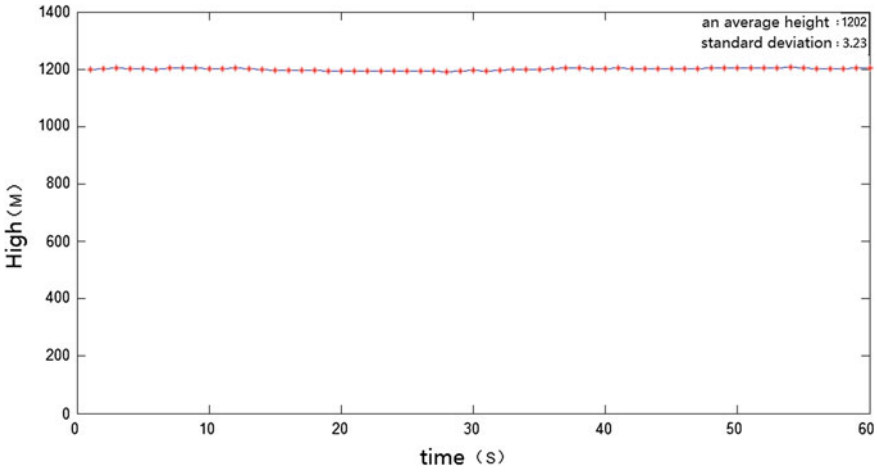

Fig. 15 Answer

References

1. Wang X, Cui H, Fu Y et al (2002) GNSS-R marine remote sensing technology. In: Twenty-fifth national conference on space exploration
2. Martin-Neira M, Caparrini M, Font-Rossello J et al (2001) The PARIS concept: an experimental demonstration of sea surface altimetry using GPS reflected signals. IEEE Trans Geosci Remote Sens 39(1):142–150
3. Steyskal H, Rose JF, Steyskal H et al (1988) Digital beamforming for radar systems. Microw J 32(1):121–123

GPS Radio Occultation Inversion Analysis of Neutral Atmospheric Detection Technology Based on Dual-Frequency Dual-Mode GNSS Occultation Receiver

Lu Zhang, Xingguo Li, Fenghui Li, Junbo Han, Qijia Dong, Yingna Liu and Meng Wang

Abstract Compared with the traditional radio atmospheric detection and radar detection, GNSS occultation technique provides a powerful tool for atmospheric detection, the GNSS occultation technique which has the characteristics of without calibration, all-weather, high precision, high vertical resolution, and global uniform coverage. The GNSS occultation technique based on the atmosphere GPS/LEO radio occultation, GPS satellite radio signal is obscured by Earth's atmosphere, GPS satellite radio signal cutting the Earth's atmosphere and ionosphere sectional, then the radio signal refracted before reach LEO satellites. The received GPS signal contains information of the Earth's atmosphere and ionosphere. We can get atmospheric and ionosphere electron density profile, the total electron content of the ionosphere and atmospheric bending angle profiles, index of refraction, temperature and barometric pressure through the relevant atmospheric inversion model. This paper introduces GPS radio occultation atmospheric detection technology based on mountain-based experimental verification, test is located at Wuling Mountain Peak of Yanshan Mountains (located in Chengde in Hebei Province, 117.48°E, 40.60°N, ~2118 m), and made a detailed presentation for signal capture, signal track, and data quality. Different from prediction algorithm of spaceborne occultation, the test used the mountain-based occultation prediction based on the fixed position, getting the forecast results of a week about occultation event. Because of mountain conditions and other factors, occultation signal capture is different because of different azimuths, and made a comparison between different azimuths making a analysis against signal to noise ratio (SNR), the consistency between the Carrier phase and the pseudorange, the reason of signal loss of lock. In order to verify the accuracy of GPS radio atmospheric occultation, this article compares the refractive index profile obtained by inversion with meteorological data, test results were better than 5 %.

Keywords GPS radio atmospheric occultation · Refractive index profile · Inversion algorithm · Meteorological data

L. Zhang (✉) · X. Li · F. Li · J. Han · Q. Dong · Y. Liu · M. Wang
Germany Space Star Technology Co., Ltd., Beijing, China
e-mail: zhanglumengcun@163.com

J. Sun et al. (eds.), *China Satellite Navigation Conference (CSNC) 2016 Proceedings: Volume I*, Lecture Notes in Electrical Engineering 388,
DOI 10.1007/978-981-10-0934-1_5

1 Introduction

GNSS radio occultation technique is a remote sensing technology detecting the Earth's ionosphere and the atmosphere through the occultation phenomenon between GNSS Navigation Constellation—Earth—LEO satellite [1], the GNSS occultation detection schematic diagram is as shown in Fig. 1.

GNSS occultation receiver can be used to carry out radio occultation observations for GPS/BD2 navigation constellation, to acquire the ionosphere environment information of the global region, including ionospheric electron density profile, ionospheric total electron content contour, atmospheric bending angle, refractive index, temperature, pressure, humidity, etc.

The inversion product of GNSS occultation detection system is the ionosphere and neutral atmosphere parameters, ionosphere inversion product including ionospheric electron density profile and ionospheric scintillation index; neutral atmospheric inversion products including atmospheric refraction ratio, density, pressure, temperature, and humidity profiles [2]. Mountain-based test, as a ground validation method of GNSS occultation detection, can provide technology and experience for spaceborne GNSS occultation exploration, this paper introduces a kind of experimental verification of mountain-based GPS atmospheric occultation technique, to support space-borne GNSS occultation exploration.

2 Section Heading GPS Occultation Detection Technology of Atmospheric Mountain-Based

2.1 GPS Occultation Forecast Mountain-Based

Occultation event occurs depends on the geometric positional relationship of GPS and LEO satellites. The occultation if exists, It is necessary to forecast occultation events and input the forecast result to receiver. Then the receiver can be acquisition and tracking occultation signal. As shown in Fig. 2 is the occultation forecast schematic.

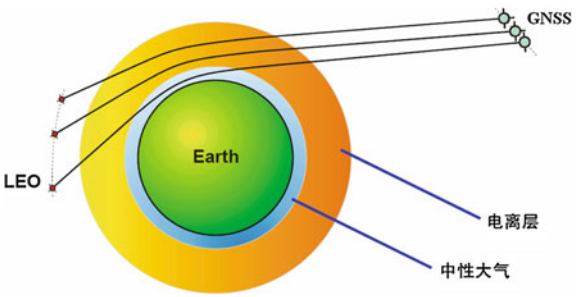

Fig. 1 Radio occultation schematic